# CORRELATIONS BETWEEN GEOMETRIC AND MATERIAL PROPERTIES OF VERTEBRAL BODIES AND THEIR COMPRESSIVE STRENGTH

# CORRELATIONS BETWEEN GEOMETRIC AND MATERIAL PROPERTIES OF VERTEBRAL BODIES AND THEIR COMPRESSIVE STRENGTH

By

JENNIFER A.E. STENEKES, B.ENG.S.

A Thesis

Submitted to the Faculty of Graduate Studies

in Partial Fulfillment of the Requirements

for the Degree of

Master of Applied Science

McMaster University

Master of Applied Science          McMaster University

Mechanical Engineering          Hamilton, Ontario

| | |
|---|---|
| TITLE: | Correlations Between Geometric and Material Properties of Vertebral Bodies and their Compressive Strength |
| AUTHOR: | JENNIFER A.E. STENEKES, B.ENG. |
| SUPERVISOR: | Dr. Mehran Kasra |
| NUMBER OF PAGES: | xi, 96 |

# Abstract

Osteoporosis is a disease characterized by reduced bone strength leading to an increased fracture risk. Current diagnostic best practice involves measuring the bone mineral density (BMD) of a patient using absorptiometric imaging tools. This measurement is compared to a known value in order to compute fracture risk. This assessment of bone quality is based solely on the BMD, which has been shown to make up only a portion of the explanation of bone strength. The extent of BMD's contribution to bone strength is also extensively debated and widely varying in the scientific literature.

This thesis work encompasses a preliminary investigation into factors in addition to density that contribute to bone strength. The geometric and material properties of 21 vertebral functional unit specimens were measured using dual energy absorptiometry (DXA), pQCT (peripheral quantitative computed tomography) and HCT (helical computed tomography) techniques. The strength of the functional units was assessed through mechanical testing under compressive loading conditions.

These measurements were amalgamated into multiple linear regression models to characterize vertebral strength in terms of a few key variables. The model developed for failure load had a coefficient of determination of 0.725 and indicated that the volume of the vertebral body as well as the cross-sectional area of the cortical

region were significant in the explanation of failure load.

A model was also developed for stress at failure which indicated that the vertebral body height and cortex concavity were important parameters. The coefficient of determination for this model was 0.871. The goal of this study was to provide a foundation on which further investigation into the explanation of bone strength could be built. Ultimately, a better understanding of the parameters that affect bone strength will provide a basis for more accurate clinical tools for the diagnosis of osteoporosis.

# Acknowledgements

The decision to pursue my Master's degree may have been solitary, but the road to its completion certainly was not. I am eternally grateful to everyone who helped me along the way, from the experts who provided technical knowledge to the friends and family who listened to my struggles and gave heartfelt advice. There are many individuals to whom thanks must be expressed individually, for without them, this work would not have been possible.

I am appreciative of the opportunity to study within the Mechanical Engineering department at McMaster, and I thank Dr. Mehran Kasra for providing me with a challenging and rewarding thesis project to work on.

I am also grateful to Dr. Philip Koshy for his support as well as his astute observations and clever questions which significantly improved the quality of my thesis. Additionally, there were many classmates who provided friendship and a sounding board for ideas. Thanks in particular to Mr. Ian Menzies and Mr. Youssef Ziada for their insightful advice.

I would like to extend my thanks to Mr. Howard Hollingham, Ms. Lesley Beaumont, Ms. Cheryl Leonard, Ms. Annette Hornby, Ms. Marilyn Kereliuk, Ms. Chantal Saab, Ms. Joanne Tutolo, Mr. Patrick Emond, Dr. Christopher Gordon and Dr. Dean Inglis, all of whom all played vital roles in the imaging portion of my study.

Special thanks to Dr. Colin Webber for introducing me to all of these amazing people and for always having an open door when I needed to discuss a new challenge I was facing. Your help was appreciated more than you know.

I greatly appreciate the assistance of Mr. Glen Oomen and Ms. Sarah Beech in sectioning my specimens and for providing the resources of McMaster's anatomy lab. Thank you to Mr. Jim McLaren for teaching me how to use a lathe and for helping me to make fixtures that seemed to undergo endless iterations. Thanks as well to Mr. Doug Culley and Mr. Ed McCaffery for their advice on compression testing and willingness to jump in and provide assistance whenever the machine acted up. I would also like to express my gratitude to Mr. Cory Minkhorst, a summer student whom worked side by side with me to complete the compression tests under grueling time constraints.

To my wonderful husband, Jeremiah, what can be said: You set the grad school example and I wouldn't have made it through without you. I am grateful for your ability to provide insight on any technical challenge, and for your excellent drawing skills in a schematic crisis. You always listened when I needed advice and support and never showed signs of being weary. You encouraged me every step of the way and taught me not to limit myself. I have learned so much from you. You are a true engineer.

This Master's has forced me to face challenges I may never have otherwise, and

has provided the opportunity to learn many things, technical and otherwise. The gifts of this experience will be carried with me throughout my life and will surely be invaluable as I begin the next phase of my career  It has been said that I tend to take the hard road, but I've truly learned that the things that are difficult are the things worth doing.

*"I have little patience with scientists who take a board of wood,*

*look for its thinnest part, and drill a great number of holes where*

*drilling is easy."*

*Albert Einstein*

# Contents

# List of Tables

# List of Figures

# CHAPTER 1
# Introduction

The alarming statistics regarding the incidence of osteoporosis in the Canadian population have triggered a vigilant effort towards better prevention, diagnosis and treatment of this costly and crippling disease. The spine is a critical structure in the body that is commonly affected by osteoporosis, leading to painful vertebral compression fractures (VCF), disability and diminished overall health.

The current diagnostic procedure relates measured bone density to fracture risk by employing absorptiometric imaging techniques to make clinical measurements. Concern has arisen both in research and clinical circles that this single parameter is not an effective surrogate of bone strength. *Ex vivo* studies [1–10] relating bone density to vertebral strength in compression have corroborated this sentiment and provided the impetus for more in-depth examination of the factors that contribute to bone strength.

The integration of a single geometric parameter with density [4, 8, 10] was shown to improve the explanation of bone strength and served as the motivation for the current study, in which multiple geometric parameters were explored and incorporated into a more complete explanation of vertebral strength. These geometric parameters are readily measurable using existing clinical tools and were shown to significantly

improve the explanation of both vertebral failure load and stress at failure.

## 1.1   The Spine

The spinal column is a vital structure in the human body  It supports the torso and extremities, protects the spinal cord and anchors critical muscles and ligaments, all the while being flexible enough to allow for movement of the torso and head [11] The human spine is made up of 24 vertebrae separated by intervertebral discs.  It is divided into cervical, thoracic, lumbar and sacral regions (Figure 1 1)
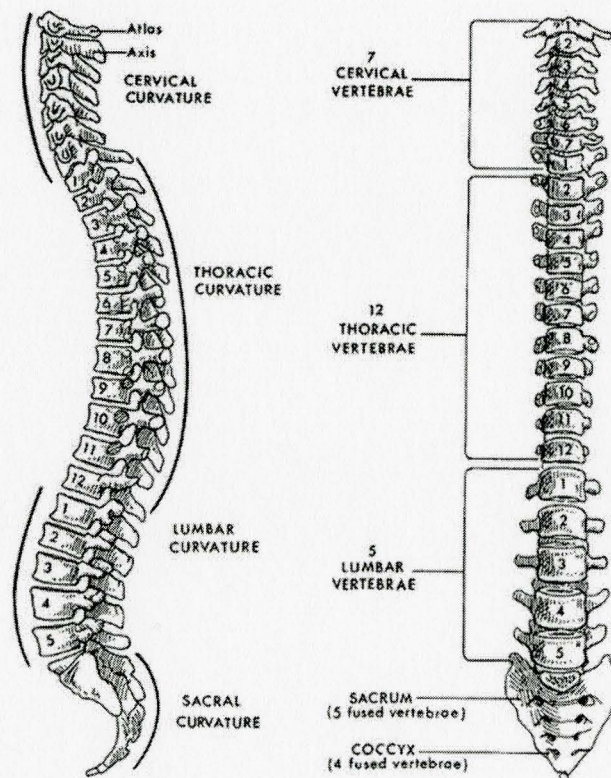


Figure 1 1  Anatomy of the spine [12]

## 1.1 1    The Vertebrae

The vertebrae are composed of several integral structural elements (Figure 1.2)

The vertebral body (or centrum) is the largest part of the vertebra. The pedicles are

short, thick pieces of bone that are located on either side of the dorsal surface of the

vertebral body  Together, with the laminae (which extend back from the pedicles),

the neural arch is formed. This region is called the intervertebral foramen and serves

as housing for the spinal cord. The spinous and tranverse processes project back from

the laminae and pedicles and serve primarily as muscle and ligament attachment sites

[13]  The facet joints are located on the left and right posterior side of each vertebra.

They are each comprised of superior and inferior articular processes, which work in

pairs to restrict the shear and torsional movements of each vertebral segment [12].
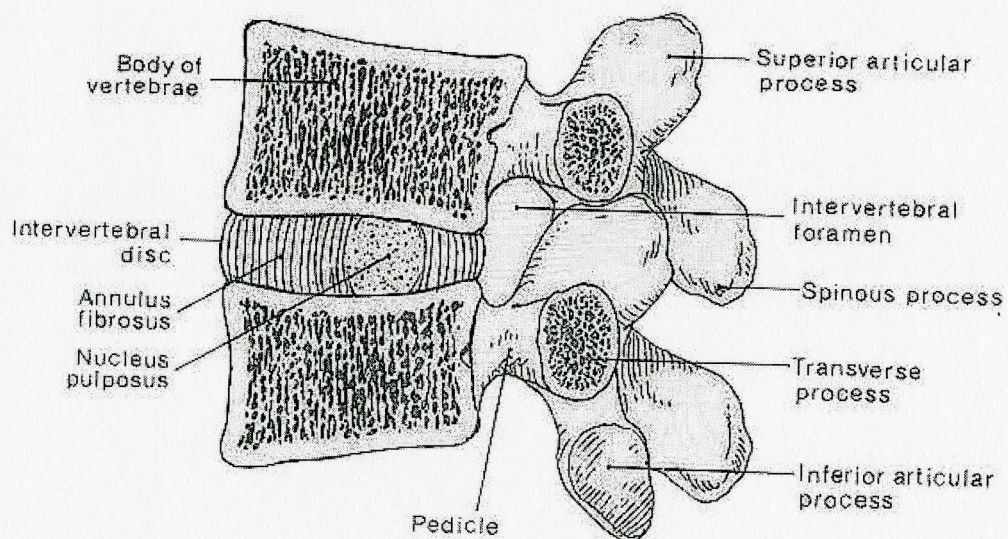


Figure 1 2: Vertebra and disc anatomy (sagittal plane) [12]

Cancellous bone makes up the majority of the vertebral body. The cancellous region has a very large surface area as it is made up of a network of trabeculae (rod or plate-like bone structures) that are aligned along lines of predominate stress in the vertebra. The trabeculae are interspersed with marrow including blood vessels and progenitor cells [14]. The cancellous region is surrounded by a thin layer of densely packed cortical bone, which has less surface area and is less metabolically active than cancellous bone [15]. Finally, each vertebral body is bounded at the superior and inferior ends by cartilignous component known as endplates, which are typically less than 0.5 mm thick [12].

### 1.1.2 Intervertebral Discs

Intervertebral discs are avascular, cartilaginous structures located between each vertebra. The discs allow articulation of the spine with movement in flexion, extension and rotation [11] while bearing a considerable amount of the load due to muscular forces and gravity [12]. The discs are made up of an inner structure called the nucleus pulposus and an outer ring-like structure called the annulus fibrosus (Figure 1.3). The nucleus pulposus is comprised of a randomly oriented collagen matrix filled with strongly hydrophilic proteoglycan gel. Lamellae made of type I and type II collagen are arranged concentrically to make up the annulus fibrosus. The amount of type I collagen is greatest in the outer lamellar layers, and decreases towards the nucleus pulposus. The opposite trend holds for the amount of type II collagen [12].
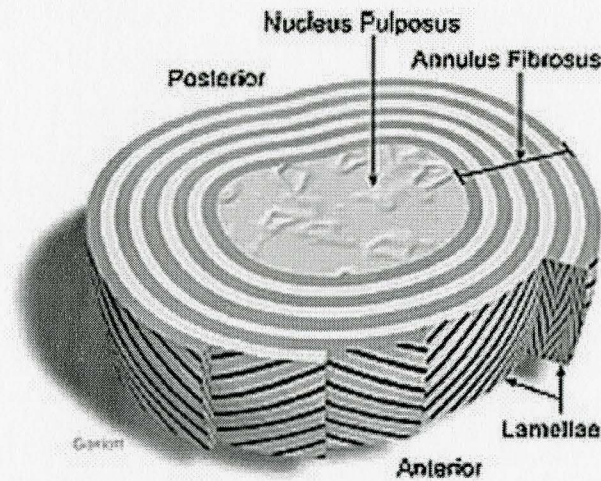
Figure 1.3: The intervertebral disc [11]

## 1 1.3    Composition of Bone

Bone serves as the chief structural element of the human body [12]    It is a connective tissue made up of cells, an extracellular matrix (ECM) and an inorganic, mineralized component ($\sim$ 55-65% by volume)    The ECM is made up of a fibrous organic element ($\sim$ 25% by volume) known as osteoid [16]    Roughly 90% of the matrix is composed mainly of type I collagen fibrils, with the remainder consisting of various noncollagenous proteins, proteoglycans and phospholipids [15]    Hydroxyapatite and calcium phosphate make up the bulk of the inorganic mineral component of bone and provide rigidity and strength. Hydroxyapatite is composed of crystals roughly 50-100 angstroms in length which are arranged in an orderly manner throughout the matrix, surrounded by amorphous calcium phosphate [12]    The three primary bone cells are osteoblasts, osteoclasts and osteocytes. Osteoblasts are cuboidal cells that pack

together into a sheet, on regions of the bone surface during active bone formation. Osteoblasts are responsible for bone formation by the creation and secretion of osteoid, as well as its eventual mineralization [12]. Osteoclasts are multi-nucleated cells that facilitate bone resorption. These cells arise from the bone marrow and are directed by a series of biochemical signals to the bone that is to be broken down. The lifespan of a mature osteoclast cell is about 35 days, at which time it experiences programmed cell death [14]. Osteocytes are inactive osteoblasts that are located inside mineralized bone [16]. They are the most plentiful type of bone cell and while their role is not well understood, they are thought to sense mechanical strain [14].

### 1.1.4   Mechanical Behaviour of Bone

Generally, both cortical and trabecular bone are stronger under compressive loading, rather than when experiencing tensile or shear forces [16].  Bone is an anisotropic material owing to the directionality of the hydroxyapatite crystals in the ECM. In cortical bone, the longitudinal orientation of the collagen fibers and osteons also contribute to its anisotropic behaviour. Additionally, bone exhibits viscoelastic properties which cause strain rate sensitivity. The viscoelastic phenomenon is a result of frictional fluid effects in the ECM that cause a portion of the elastic energy to be dissipated. Despite this, bone is often modeled as an elastic material in order to simplify stress analysis [17]. Some investigators have chosen to examine the individual material properties of different types of bone. These studies have revealed that the

Poisson's ratio (ratio of lateral to axial strain) for cancellous bone is typically between 0.2 and 0.3 [14]. A study by Ashman et al. [18] found values between 0.28 and 0.45 for Poisson's ratio of cortical bone. According to studies described in An et al. [15] the stress at failure in compression for cortical bone ranges from 133 to 195 MPa while the elastic modulus is between 14.7 and 34.3 GPa. These values for cancellous bone range from 1.5 to 38 MPa for ultimate stress in compression and between 10 and 1570 MPa for the elastic modulus.

## 1.2   Osteoporosis

In the mid-1800's, the term 'osteoporosis' was coined to describe the evident porosity of elderly bone [14]. While the association between osteoporosis and low bone density has held on over the years, it has become evident that many factors besides bone mineral density contribute to the fracture risk of bone. This has led to a shift in the way in which osteoporosis is regarded and a new definition of the disease was developed to reflect this change. In the year 2000, the National Institutes of Health Consensus Development Panel redefined osteoporosis as "a skeletal disorder characterized by compromised bone strength predisposing to an increased risk of fracture" [19] commonly affecting the spine, hip and wrist. Canadian statistics indicate that 1 in 4 women and 1 in 8 men are currently affected [20] at a cost expected to reach $2.4 billion annually by the year 2041 [21]. As the proportion of the population over the age of 50 increases, the number of people with osteoporosis will continue to

grow  This is compounded by the fact that the incidence of osteoporotic fractures is increasing more quickly than the number of people in the elderly segment of the population [20]

### 1.2.1  Characteristics and Incidence of Vertebral Compression Fracture

There are two predominant types of vertebral fractures observed in osteoporotic patients (Figure 1.4)  A wedge fracture is characterized by a marked decrease in the anterior height of the vertebral body while in a crush fracture there is a decrease in both the anterior and posterior height of the vertebral body  Clinical evidence has shown that vertebral fractures occur most frequently in the mid-thoracic (T7-T8) and the thoracolumbar (T12-L1) region of the spine [22]
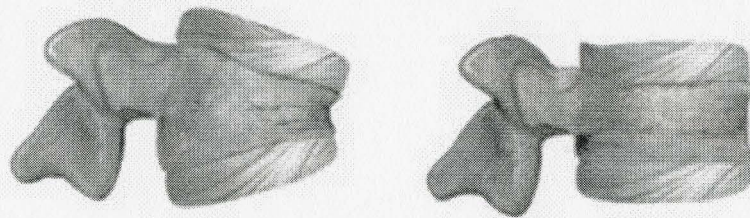


Figure 1.4. Vertebral wedge fracture (left) and vertebral crush fracture (right) [23]

Vertebral compression fractures are typically accompanied by acute pain at the time of fracture followed by chronic pain at the fracture site and in the surrounding trunk structures that shift to accommodate the vertebral deformity  This can impair breathing and mobility resulting in a diminished quality of life [24]  A study by

Lindsey et al. [25], showed that 83% of vertebral fractures are caused by trauma considered "moderate or less". This is defined as being less than, or equal to falling from standing height. Day-to-day activities such as carrying groceries, bending over to lift an object or even sneezing can cause a vertebral fracture. The incidence of vertebral fracture is relatively common. Cooper et al. [26] studied the number of vertebral fractures in Rochester, Minnesota between 1985 and 1989 and found the rate for women (153/100,000 per year) to be comparable to the rate of hip fracture for both sexes (114/100,000 per year). The incidence of vertebral fracture in men (81/100,000 per year) was about half that of women.

### 1.2.2  Clinical Diagnosis of Osteoporosis

Early and accurate diagnosis of osteopenia (pre-osteoporosis) and osteoporosis itself are critical as there are a variety of effective treatment options available. Medications that alter the rate of bone turnover, microstructure and mineralization of bone have all been shown to reduce fracture risk [27, 28]. Additionally, it has been determined that pharmaceuticals are most effective prior to the disease causing perforation of entire trabeculae [29]. Currently, measurement of bone mineral density (BMD) by dual energy absorptiometry (DXA) is the clinical gold standard for diagnosing osteoporosis [30]. A given patient's BMD is compared to those for a young, healthy adult of the same gender and the difference is conveyed as a standard deviation score known as a "T-score" [31]. The World Health Organization defines a

T-score of -2.5 as osteoporotic [27]. Studies have shown that the T-score standard is not always an effective measure of fracture risk. The National Osteoporosis Risk Assessment study examined 149,524 postmenopausal females over the course of 1 year. During this timeframe, 2259 patients experienced osteoporotic fractures. Of these, 82% of patients had T-scores greater than -2.5 [32]. Additionally, the multicenter Study of Osteoporotic Fractures indicated that a baseline central T-score of greater than -2.0 was measured in 54% of patients who suffered non-vertebral fractures [33]. This evidence indicates that current T-score measurements are underestimating the actual fracture risk of patients with or without prior osteoporotic fractures.

## 1.3 Noninvasive Bone Measurement Techniques

At present, measurement of bone strength can only be achieved through mechanical testing. Since this is not possible with living patients, non-invasively attained parameters must serve as a proxy measure of strength. Several different devices have been developed to assist in the determination of the bone mineral content and geometric properties of bone. Two of the most widely used classes are those using absorptiometric techniques and computed tomography techniques. Absorptiometric techniques such as dual photon absorptiometry (DPA) and dual x-ray absorptiometry (DXA) measure bone mineral content over a projected area, giving a two-dimensional measure of bone density known as areal bone mineral density (aBMD). Alternatively, computed tomography techniques including pQCT (peripheral quantitative computed

tomography) and HCT (helical computed tomography) are capable of generating a

three-dimensional measure of bone mineral density, as the bone mineral content is

attained for a cross section of known area and thickness. It is important to note

that density calculated in absorptiometric techniques is an apparent or Archimedean

density, meaning that the entire bone substance including cells, marrow etc. is in-

cluded in the area measurement [15]. Conversely, in volumetric techniques, only

voxels with attenuation coefficients corresponding to bone are included in the bone

area measurement. Therefore, the density measurement acquired using pQCT is a

truer measurement of bone density. Regardless, DXA is the more widely used clinical

technique since it exposes the patient to a lower radiation dose and has a faster scan

time than pQCT. A summary of the characteristics of DXA and pQCT as adapted

from Augat et al. [34] is shown in Table 1.1.

Table 1.1: Characteristics of DXA and pQCT.

| Technique | Radiation Dose ($\mu$SV) | ScanTime (min) | Resolution (mm) |
|-----------|--------------------------|----------------|-----------------|
| DXA       | 20 - 30                  | 3 - 6          | 1.5             |
| pQCT      | 30 - 100                 | 6 - 10         | 0.25 - 0.68     |

## 1.3.1  Dual Photon Absorptiometry and Dual X-Ray Absorptiometry

The development of dual photon absorptiometry in the late 1970's permitted

bone content measurements in anatomical areas of varying thickness and composition

such as the axial skeleton and hip [34, 35]. In this technique, two radionuclides

emanate gamma radiation at differing characteristic energy levels and are positioned

in such a way that a collimated beam is created and directed at the area of interest

[36]. The attenuation of the two energy peaks are measured and, through the use of

a calibration phantom, the bone mineral content for that area is determined [34].

Dual energy x-ray absorptiometry was commercially launched in 1987 as the

successor to DPA. The operating principle for DXA is the same as DPA except that

instead of a radionuclide source, x-rays of two different energy levels are used. Devel-

opment of dedicated computer software allowed the projectional area of the vertebra

to be determined. Typically, an edge detection algorithm is used to process the slice

image. The algorithm distinguishes the change from soft tissue to bone by examining

density gradients, thus creating a "bone map" [37]. The number of pixels inside the

bone map can be calculated and converted to a projectional area measurement. Fi-

nally, the aBMD is found by dividing the bone mineral content by this area. Due to

an increased photon flux of the x-ray tube, patient examinations using DXA can be

performed in significantly less time than with DPA. Additionally, DXA is more ac-

curate and precise than DPA because there is no half-life decay of the energy source

and a greater image resolution is attainable [35]. First generation DXA machines

used a pencil beam x-ray source and took between 6 and 15 minutes to execute a

single examination scan. Newer fan beam devices have reduced this time to around 2

minutes [38]. A review paper by Genant et al. [35] reported the *in vivo* precision of

DXA measurements of the lumbar spine as 0.5-1.5% while the accuracy error ranged from 5-10%. DXA has become the most widely accepted bone density measurement tool since it is straightforward to use, has a comparatively low cost and exposes the patient to a very low radiation dose. There are several limitations to this technique though, when it is being used as a surrogate of bone strength. Since DXA finds density by dividing the bone content by the projected vertebral area (usually the area of the front or rear face of the vertebrae) the effect of the patient's body size is partially reduced, but this is not reflective of the true volume of the vertebra. Additionally, areal BMD is an average density value incorporating both the contributions of the cortical shell and the cancellous centrum of the vertebra [33]. The individual contributions of these components cannot be determined using this imaging technique. Furthermore, the actual correlation between aBMD measured with DXA and bone strength has long been a point of contention in the scientific literature, as will be further discussed later.

### 1.3.2  Quantitative Computed Tomography

In quantitative computed tomography (QCT), x-ray projections are taken at equally spaced angular positions around the circumference of an object. These projections are created by measuring the attenuation of the x-rays through the specimen and reconstructing them into a cross-sectional image (slice) of the object. Since the slice has a predetermined thickness, each pixel in the image actually corresponds to

a volume unit called a "voxel" The number of voxels in a given field is a characteristic value for the machine, indicating its resolution [15] The area used for density calculation in pQCT is a cross-sectional area of the vertebra, as shown by the shaded region in Figure 1.5.
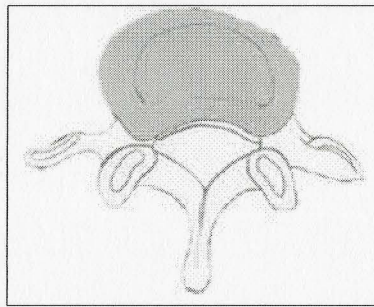


Figure 1.5: Area determined by pQCT

Through the use of a calibration phantom, the attenuation coefficient for each voxel is converted to a bone mineral content for the area of interest, in $mg/cm^2$ By dividing this value by the thickness of the image slice, the volumetric bone mineral density, in $mg/cm^3$, can be found. The advantage of pQCT over DXA is that it allows a true volumetric density measurement to be made without obstruction by other tissues or structures. Additionally, the exact three-dimensional location of the measured region can be determined [35] The accompanying software also allows for separate density measurement of the cortical and trabecular bone, as well as several geometric parameters. In vivo precision errors were evaluated in a study by Butz et al. [39] A relative error of 1 7% was determined for trabecular BMD measurements, 0.9% for cortical BMD measurements and 0.8% for overall BMD measurements [39] In recent

years, peripheral quantitative computed tomography evolved as a high resolution,

small field successor of QCT machines.

### 1.3.3   Helical Computed Tomography

Helical computed tomography first emerged on the market in 1989 as a new

approach to volume acquisition using x-ray computed tomography  Rather than being

limited to the 360° circumference around the object, helical CT operates by taking

contiguous projections as both the x-ray source and detector travel on a helical path

while the table moves through the gantry opening (Figure 1.6) [40]
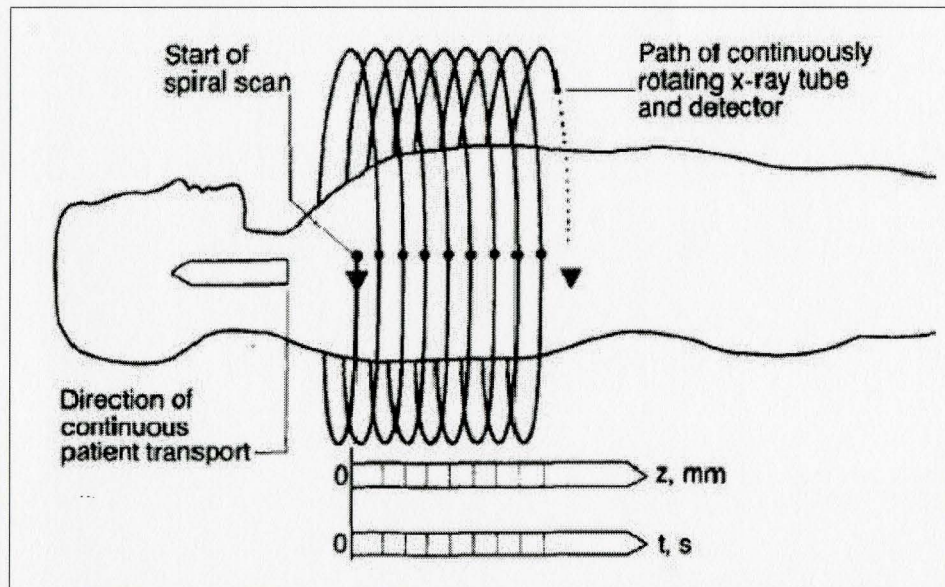


Figure 1.6: Schematic of operating principle used in helical computed tomography [40]

Due to the speed with which the entire volume can be scanned, it is possible

for a patient to hold their breath for the length of the scan. This greatly reduces the

gaps or irregularities in the image due to patient movement or breathing that would

be observed on a traditional CT scan [40]

In summary, the current clinical protocol for the diagnosis of osteoporosis relies on areal bone mineral density as determined by DXA as a proxy measurement of bone quality. It has been shown clinically that a large proportion of patients who were classified as having non-osteoporotic bone quality in this manner actually suffered osteoporotic fractures, illustrating the shortcomings of the current approach.

The development of volumetric imaging techniques such as pQCT and HCT facilitated the acquisition of more detailed densitometric and geometric information, allowing the study of these parameters in relation to bone strength. The hypothesis of the current study was that the inclusion of these geometric and densitometric measurements attained by volumetric imaging techniques would improve the explanation of bone strength as measured by mechanical testing.

# CHAPTER 2
# Literature Review

The pursuit of a more complete understanding of the factors that contribute to vertebral strength has prompted the clinical and laboratory study of the human spine. The evolution of mechanical testing methodologies have allowed the *in vivo* loading conditions experienced by vertebrae to be simulated in the laboratory while the use of absorptiometric imaging tools has allowed density measurements of the different types of bone in the spine to be assessed as well as (to a limited extent) quantifying geometric characteristics of vertebrae.

## 2.1  Assessing the Compressive Strength of Vertebrae

Many researchers have attempted to ascertain the strength of vertebrae by mechanically testing cadaveric specimens. Due to the wide variation in human anatomy and physiology, the challenge of creating an accurate and repeatable *in vitro* test which correctly portrays the *in vivo* condition is not a trivial task. Additionally, it is very difficult to simulate the role of muscle forces and soft tissue during bone loading in the testing environment. For these reasons, researchers generally choose to conduct experiments which have simplified loading conditions, such as uniaxial compression. The conditions and assumptions associated with uniaxial compression are acceptable when the study focuses on the properties of the vertebral body, since pure compres-

sive forces are predominantly transmitted through the vertebral body. The posterior elements play a greater role in force transmission during combined compression and torsional loading as well as in pure torsion and rotation [41].

### 2.1.1 Approaches to Compression Testing

A common technique for vertebral compression testing involves testing only a single vertebral body, with or without the posterior elements. This approach is appealing because it reduces the anatomical complexity of the study. Many variations on the single vertebra technique have been employed during investigations of bone strength. Some researchers simply placed the specimen between two parallel plates and applied a compressive load [3, 5, 41]. Eriksson et al. [42] used high viscosity bone cement on either end of the specimen such that a level load application surface was created. Singer et al. [8] furthered this technique by testing the specimen in a temperature and humidity controlled environment in order to simulate conditions found in the human body. This setup produces difficulty in creating a level load application surface due to the limited specimen size. Furthermore, the load transferring properties of the intervertebral disc are not taken into account. In an effort to counteract this effect, Cheng et al. [10] inserted a rubber sheet between the specimen and the loading platen in order to simulate the effect of the intervertebral disc (Figure 2.1). The drawback of this method is that it treats the intervertebral disc as a uniform material, which it is not. The disc is comprised of an annulus fibrosus and a

nucleus pulposus, each having distinct material and mechanical properties. Using a single material to simulate a disc may also neglect important endplate effects on the trabecular bone.
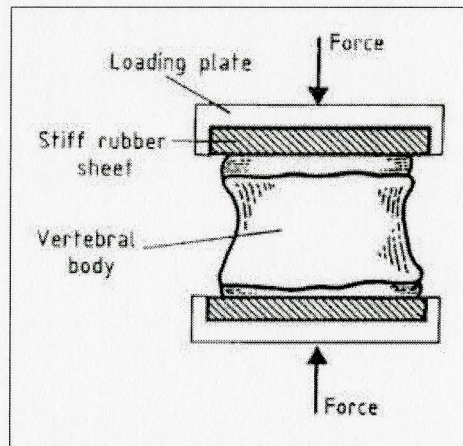


Figure 2.1  Example of single vertebra compression test [10]

An approach taken by Hasson et al. [6] left a 3-mm thick slice of disc intact on either endplate of the specimen. In this case, the intent was to standardize the effect of the disc by controlling its thickness while retaining (to some degree) its load transmission properties.

As the importance of the disc in transferring load became more apparent, many investigators elected to test sections of spine consisting of two or three vertebrae in order to allow the disc to act more as it would in the *in vivo* situation. Brinkman et al. [1] tested two vertebral bodies with one intervertebral disc between them (Figure 2.2)  In this configuration, the load was transferred to the inferior vertebra through the disc but the loading on the superior vertebra was directly applied, as in the single

vertebra test case.
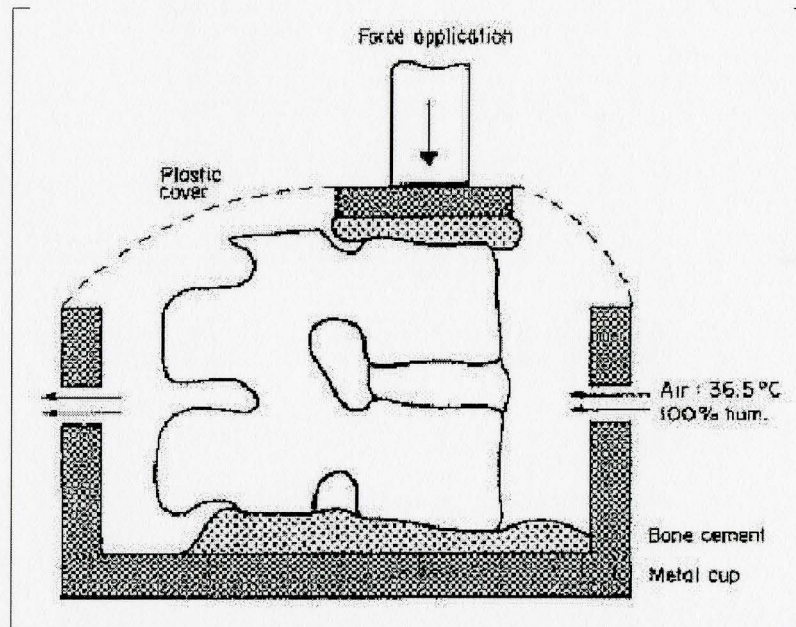


Figure 2.2: Two vertebrae approach used by Brinckmann et al. [1]

The "functional unit" or 3 vertebrae/2 disc specimen has been used by many researchers [4, 7, 43] in order to transfer load through the specimen in a physiological manner (Figure 2.3)  Typically, the vertebrae on either side of the target vertebra were embedded in high viscosity bone cement, usually polymethylmethacrylate (PMMA)  This created both a level load application surface and ensured that the fracture occurred in the target vertebra.  This allowed the *in vivo* situation to be much more closely reproduced as the load is transferred through the reinforced vertebra, then to the disc, then to the target vertebra.  Additionally, the presence of the intervertebral discs on both ends of the target vertebra gives the functional unit some ability to flex and adjust to the load as it would in the body
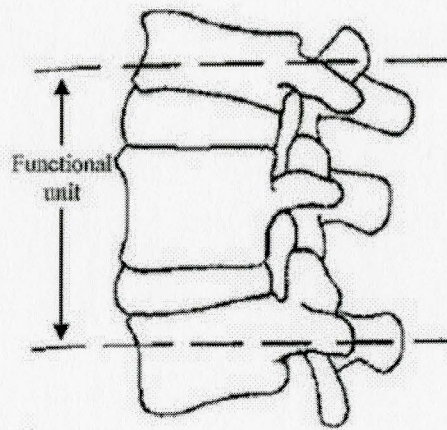
Figure 2.3. Vertebral functional unit [9]

### 2.1.2   Comparison of Measured Values to *In Vivo* Loads

It is difficult to determine whether the strength found by testing a single vertebra

or a functional unit is closest to the *in vivo* value as both techniques produce a broad

range of values for the failure load, typically ranging from 2 to 9 kN [1, 2, 8, 10]  This

wide span of measurements makes it difficult to separate the natural variation between

specimens from the effect of applied testing conditions, such as simulated *in vivo*

temperature and humidity levels. Nachemson et al. [44] evaluated *in vivo* vertebral

loads by measuring the intradiscal pressure experienced by subjects in various quasi-

static postures. Results of this study revealed loads of up to 2 kN were characteristic.

Leskinen et al. [45] measured loads experienced by subjects lifting a 15 kg object and

found values between 2 and 4 kN  These measured *in vivo* loads give credibility to

the experimentally determined *ex vivo* failure loads, which typically fall at the higher

end of the range given. This is a logical finding as the *ex vivo* loads are measured at

failure and therefore represent the ultimate load borne by specimen.

### 2.1.3   Rate of Load Application

Bearing in mind that bone is viscoelsastic in nature, the deformation rate selected for mechanical testing directly affects the measured failure load and other mechanical properties. Deformation rates on the order of 0.1 mm/s are typically used for quasi-static compression tests of vertebrae, resulting in a loading rate of between 0.5 and 1 kN/s [1]. A study by Kazarian and Graves [46] demonstrated that increasing the rate to between 5 and 10 mm/s resulted in a 20-30% increase in measured strength, further confirming the significance of selecting the appropriate deformation rate. Therefore, compression tests employing a deformation rate in the range of 0.1 mm/s will result in minimum loads that can be borne by the specimen, corresponding to *in vivo* spinal loading during slow movement or lifting motion [1].

## 2.2   Previous Studies

The bulk of the existing literature explored failure load or stress at failure in relation to bone mineral density. The studies outlined here will highlight the correlation values determined by different investigations and will illustrate the gap in the characterization of bone strength that is explained by measures of bone density alone. Following from this, the effect of geometric parameters and the cortical shell on bone strength were examined both in clinical and *ex vivo* studies. A few investigators

furthered this line of thinking by simultaneously relating cross-sectional area and density to strength. This literature review will demonstrate the need for further exploration of the combined effect of geometry and density on vertebral strength and will outline the objectives of the current study.

### 2.2.1   Bone Density and Strength

The correlation between bone density and the compressive strength of vertebrae has been well established, although the strength of this relationship is controversial. As early as 1966, Weaver and Chalmers investigated the relationship between cancellous bone ash density and stress, finding a degree of determination of nearly 70% [47]. This finding was corroborated by Bell et al. in 1967 [48]. One of the first studies to use noninvasive measures of bone density was conducted by Hansson et al. [6] in 1980. A strong positive correlation ($R^2 = 0.74$) was found between the bone mineral content (BMC), measured by DPA, and the ultimate compressive load of a single vertebra. Other investigators measured BMC with DXA [4, 5, 7, 8] and found a significant correlation with ultimate load. This correlation was slightly improved when BMD was related to ultimate load [3–5, 7, 8, 10]. A summary of the results of these studies is presented in Figure 2.4. Please note that when a range of $R^2$ values was given in the study, the maximum was included in Figure 2.4. Also, the BMC correlation found by Edmondston et al. [4] was not included in the average as it appears to be an outlier. A possible explanation for this anomalous result is that the specimens

used in the study by Edmondston et al. had been fixed in a formalin solution for an

extended period of time (3-4 weeks)  This may have influenced the correlation found

since it has been shown that formalin fixation slightly increases compressive strength

but does not significantly affect bone density [49]
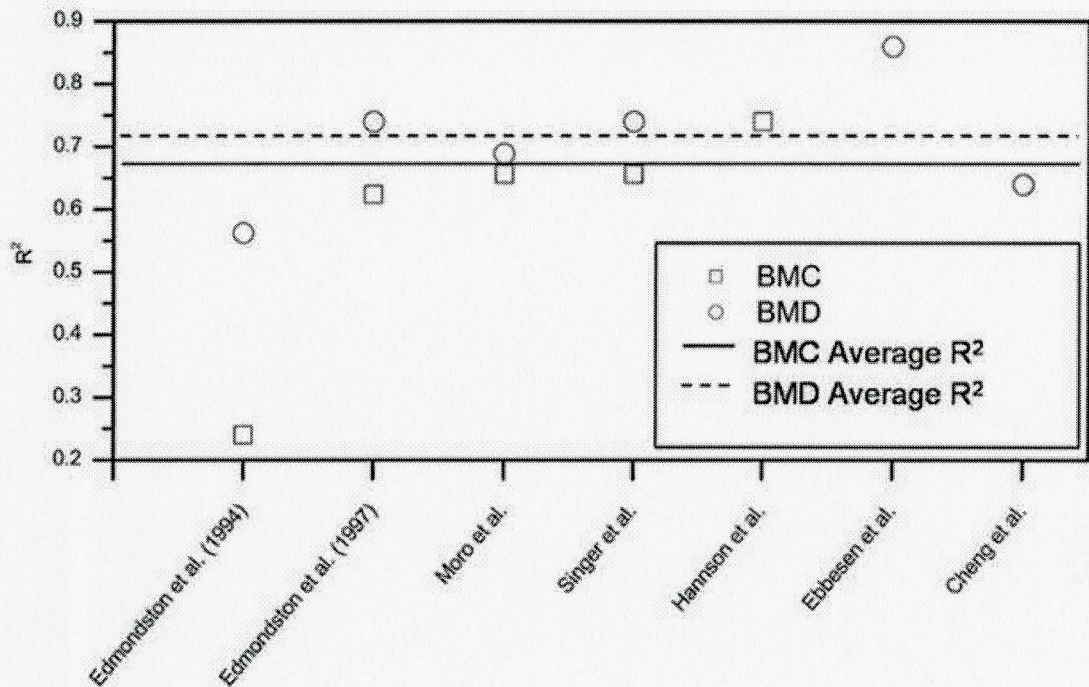


Figure 2.4. Correlations between bone content, density and failure load.

Additionally, the correlation between BMC and ultimate stress was explored.

This was generally found to be a weaker correlation than with ultimate load, but was

improved by up to about 15% when BMD was correlated with ultimate stress [4, 5],

creating a correlation between two normalized variables. Using QCT, several inves-

tigators were able to determine the density of the trabecular component of vertebral

bone [1, 2, 4, 5, 8, 10]  There was a weak correlation between trabecular density and

ultimate load, although it should be noted though that the range of values given in the literature was very broad ($R^2$ = 0.08-0.51). The correlation was slightly stronger between trabecular density and ultimate stress ($R^2$ = 0.36-0.61), but in general the coefficients of determination for trabecular density were lower than for BMC or BMD.

### 2.2.2 Contribution of the Cortical Shell to Vertebral Strength

Given that the layer of cortical bone surrounding the vertebral centrum is very thin (typically between 0.25 and 0.4 mm) [50], assessing its contribution to the strength of the vertebra is a challenging task. Studies by numerous investigators have presented widely varying values for its contribution to vertebral strength, ranging from 10-75% [43, 51]. McBroom et al. [43] attempted to evaluate the contribution of the cortical shell to vertebral strength by testing vertebral bodies with and without the cortex intact. Both groups were compressed uniaxially and the failure loads were measured. There was no significant difference between the two groups. A limitation of this study was the method by which the cortical shell was removed. Since it was ground away, it was difficult to determine if it had been fully removed or whether it may be still providing some reinforcement to the vertebral body. This may have affected the failure loads measured under compressive loading. Difficulties such as those described in the study by McBroom et al. have prompted researchers to turn to finite element analysis in order to assess the contribution of the cortical shell to vertebral strength [52, 53].

### 2.2.3   Geometry and Bone Strength

It has been recognized that the structural geometry of bone is an important factor in bone strength since the specimen dimensions govern the amount of force under loading that can be withstood [18]. Gilsanz et al. [54] conducted a study of matched women with and without osteoporotic fractures. It was found that the cross-sectional area of unfractured vertebral bodies in women who had previously suffered a fracture was, on average, 7.7% smaller than those who had not suffered a fracture. This study highlighted the significance of geometrical factors in the *in vivo* case and initiated further *in vitro* study. A study by Edmondston et al. [5] further explored the correlations between geometrical parameters and failure load of vertebrae. Results of this study showed a weak correlation between vertebral height and failure load ($R^2$ = 0.05-0.24) as well as between cross-sectional area at the midplane and failure load ($R^2$ = 0.036-0.15). A range of $R^2$ values were indicated because separate analyses were performed for each of 4 thoracolumbar regions. The effect of vertebral concavity was measured as two height ratios: anterior height/posterior height and middle height/posterior height. Both of these concavity parameters showed poor correlation with failure load.

### 2.2.4   Relationship Between Cross-Sectional Area, Density and Strength

Four studies considered the combined effect of vertebral area and density on failure load. Studies by Brinckmann et al. [1], Singer et al. [8] and Cheng et al. [10]

showed that multiplying vertebral trabecular density with endplate area or midplane cross-sectional area gave a greatly improved correlation with failure load ($R^2 = 0.61$-$0.69$) compared to vertebral trabecular density alone ($R^2 = 0.08$-$0.38$). The work by Edmondston et al. [4] indicated that multiplying trabecular density by mid-body cross-sectional area actually gave a slightly weaker correlation with failure load than trabecular density alone. Once again, the only significant difference between this study and the others is that the specimens in this case had been fixed in formalin for a lengthy period of time.

## 2.3  Scope and Objectives of Thesis Work

The presented body of evidence indicates that the factors that contribute to bone strength are not fully understood. The degree to which bone density impacts bone strength has been extensively debated in the research community and the data varies widely between studies. Regardless of the study chosen, it is clear that bone density alone is not a sufficient predictor of bone strength. Some work has been conducted on the correlation between geometrical parameters and bone strength with promising results, but the limited amount of data in this area necessitates further exploration. This thesis focused on investigating strength relationships for the spine, as this is one of the critical regions of the body in terms of osteoporotic fractures. Three non-invasive bone assessment techniques were utilized that could be applied to patients in clinic. Dual-energy x-ray absorptiometry was used to assess the areal

bone mineral density of vertebrae in the manner that is currently employed clinically. Additionally, peripheral quantitative computed tomography was used to investigate the density of different components of bone, as well as their cross-sectional areas. Finally, helical computed tomography was used to generate high-resolution images of the vertebrae such that a variety of geometrical parameters could be assessed. The strength of vertebrae were be investigated from a structural perspective with a focus on measuring strength under conditions as close as possible to those found in the human body. As opposed to investigating the individual material properties of the different components that make up the vertebrae, spinal functional units were treated as complex composite structures and were evaluated as a whole, allowing the natural interactions between the materials to remain intact.

In summary, the goal of the current investigation was three-fold:

- To clarify the relationship between bone density and strength

- To identify geometric parameters which may contribute to bone strength

- To incorporate these parameters such that the explanation of bone strength is maximized.

As the incidence of osteoporosis continues to increase due to our aging population, it is vital that a more accurate technique for the prevention and/or diagnosis of this disease be developed. The relationships established in this work will provide a

foundation which will hopefully lead to further studies in the future. Ideally, these relationships could bring about a change in the way bone strength is assessed clinically and provide a better technique for the diagnosis of osteoporosis.

# CHAPTER 3
# Materials and Methods

In the current study, the densitometric and geometric properties of human cadaveric vertebral specimens were measured using absorptiometric and computed tomography techniques. The strength of the vertebral specimens was assessed through mechanical testing in which each specimen was loaded until failure under uniaxial compressive loading conditions. Imaging techniques were also used to provide insight into the condition of the intervertebral discs and to evaluate the characteristics of the failed vertebrae after mechanical testing.

## 3.1   Materials

The spinal specimens were received in a frozen state from the University of Toledo, who had acquired them through the National Disease Research Interchange (NRDI) and had used the lumbar sections in their own biomechanical studies. Both ethical and biohazard approval were attained for the use of the specimens in the current study through the McMaster Ethics Review Board and the McMaster Biosafety Office. The 5 spine specimens generally contained 11 vertebrae from the thoracic or thoracolumbar spine. Specimen 1 was an exception as it was smaller, consisting of one section of 2 vertebrae and another section of 3 vertebrae. A description of each specimen and corresponding donor is given in Table 3.1.

Table 3.1: Specimen and donor details.

| Specimen Number | Spine Section | Gender | Age | Cause of Death |
|---|---|---|---|---|
| 1a | T12-L1 | F | 66 | Pancreatic cancer |
| 1b | T9-T11 | F | 66 | Pancreatic cancer |
| 2 | T1-T11 | F | 60 | Anoxic encephalopathy |
| 3 | T1-T11 | F | 76 | ASCVD, dementia |
| 4 | T5-L5 | M | 87 | Ischamic heart disease |
| 5 | T2-T12 | M | 71 | Meta carcinoma |

Upon receipt, the specimens were immediately placed in polyethylene bags, labeled, sealed using a commercial vacuum sealing device and stored at -20°C in the laboratory freezer.

## 3.2  Imaging

As there was a significant amount of soft tissue still intact on the specimens, all of the pretest scanning took place in air, to simulate the *in vivo* case. Unlike the *in vivo* case, it was necessary to image the specimens while frozen in order to minimize the number of freeze thaw cycles which would compromise specimen integrity and affect the mechanical testing results.

### 3.2.1  Pretest Radiological Examination

X-ray images (sagittal view) were taken of the specimens prior to commencing the formal study. These images were examined in order to ensure that there were no previously existing fractures or anomalies that would disqualify a particular specimen from the study.

### 3.2.2   Dual Energy Absorptiometry

DXA was performed on each vertebral body in the AP (front to back) view according the manufacturer's procedure. The measurements were performed by a bone density technician using a Hologic Discovery instrument. A small animal algorithm was used with an array scan mode, a resolution of 0.064 cm, a line spacing of 0.1512 cm and a scan width of 17.9 cm. Using Hologic QDR Software for Windows XP (V 12.3), a rectangular region of interest (ROI) was manually selected around each vertebral body and the BMC and scanned projectional area were measured. The software calculated aBMD for each vertebra by dividing the BMC by the projectional area.

### 3.2.3   Peripheral Quantitative Computed Tomography

pQCT imaging was performed on each vertebra using a Norland Stratec XCT-2000 scanner. A cylindrical Plexiglas tube was sectioned lengthwise and used to hold the specimens during scanning (Figure 3.1). Within the tube, the spine sections were manually propped up such that the vertebral body being scanned was approximately perpendicular to the gantry of the machine.

An anthropometric calibration phantom was scanned prior to each testing session in order to ensure measurement precision. The specimens were manually aligned such that the scan would begin near the superior end of the vertebral body. The scan process was initiated and 15 projections spaced at 24° apart were taken and reconstructed to create a cross sectional slice with a thickness of 2 mm. The gantry
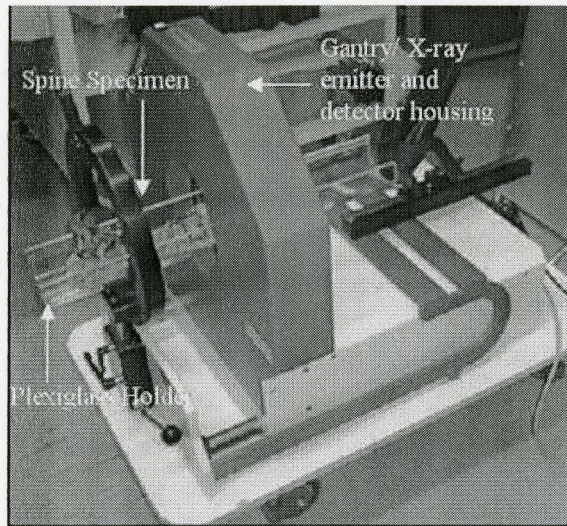
Figure 3.1  pQCT experimental set-up.

moved 4 mm away from the starting location and another sliced was scanned. This

process was repeated for each vertebra such that one slice near the superior end (slice

1) and another 4 mm away from this location (slice 2) were imaged. A rectangular

ROI was selected around each slice, bordered by the edges of the vertebral body on

the top, left and right and by the top of the spinal canal at the bottom as shown in

Figure 3.2.
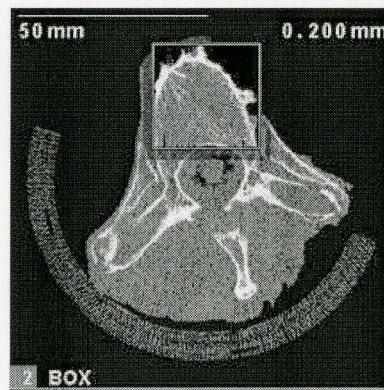


Figure 3.2: ROI selection of pQCT image.

The bone edge detection was conducted using contour mode 2 and peel mode 2 with threshold 1 set to 169 mg/cm$^3$, threshold 2 set to 400 mg/cm$^3$ and the cortical threshold set to 711 mg/cm$^3$  The voxel size for the scans was 0.2 mm. An example of the resultant regions of trabecular and cortical bone for a given slice are shown in Figure 3.3. More details on the mechanism of the bone edge detection algorithm can be found in Appendix I. Using the threshold values indicated above, the bone
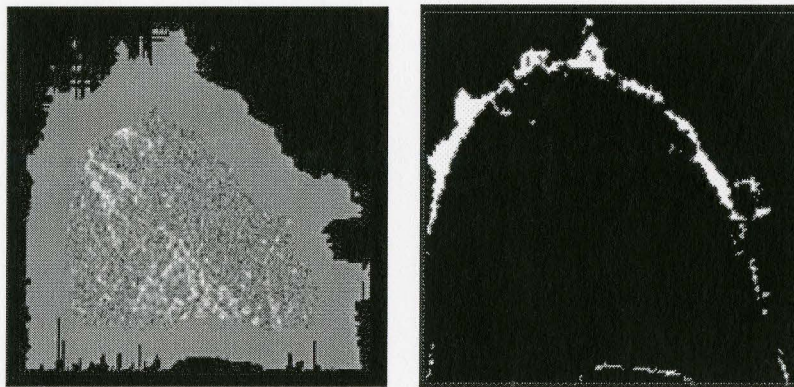


Figure 3.3. Trabecular (left) and cortical regions (right).

content per 1 mm slice (mg/mm), bone cross-sectional area (mm$^2$) and volumetric bone density (mg/cm$^3$) were found for the entire slice as well as the trabecular and cortical regions of the slice.  This resulted in 9 parameters being recorded at two different slice locations in each specimen.

### 3.2.4   Helical Computed Tomography (Pre-Test)

Each spine section was imaged using a multi-slice Toshiba Aqualion 16 detector scanner  The technologist used a bone algorithm and the machine parameters were set as follows: Slice thickness    1 mm, Interval = 0.5 mm, Pixel size $\sim$ 0.3 mm, Field

of View = 16x16 cm, Voltage = 120 kV, Current = 200 mA.

### 3.2.5 Magnetic Resonance Imaging

In order to have a visual record of the intervertebral discs, it was necessary to utilize an imaging modality that resolved soft tissue well. For this reason, magnetic resonance imaging (MRI) was performed on the thawed spine sections using an OrthOne 1T high-field peripheral scanner. The scans were performed using the following parameters: slice thickness = 1 mm, field of view = 8 x 8 cm, acquisition matrix = 256 x 128 pixels. A T2-weighting was used (TR/TE = 30/12.7 ms) with an echo train of 1.

## 3.3 Image Analysis

### 3.3.1 Correction for Angular Misalignment of CT Images

Imaging of the spine sections with HCT created slices oriented perpendicularly to the axis of the table. Due to the curvature of the spine, this created skewed slice images for some of the specimens. In order to obtain the correct slice images, new slices oriented perpendicularly to the curved axis of the spine needed to be created. Figure 3.4 illustrates by the dashed line, the slice orientation in the original HCT image (left) and the desired orientation (right).
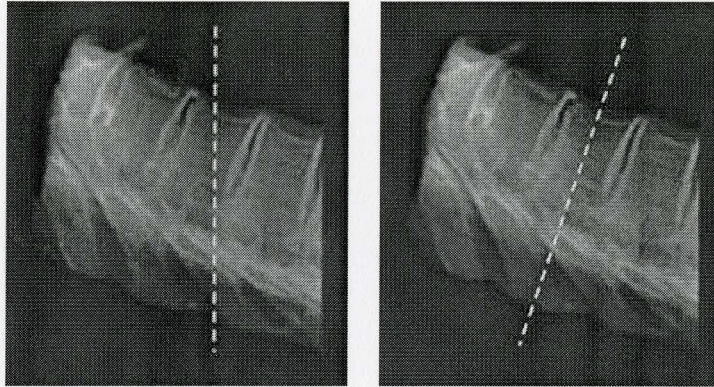
Figure 3.4: Original slice orientation (left) and desired orientation (right)

Using a software package called eFilm, a 2D sagittal view of each specimen was created. Using the multi-planar reformatting (MPR) function, new cross-sectional slices were created. By adjustment of the MPR measurement line, the slice could be oriented approximately parallel to the endplates of the vertebral body and perpendicularly to the axis of the spine as shown in Figure 3.5.

For each functional unit, a new slice (now called MPR slice) was created at each of the endplates of the vertebral body as well as at the approximate location of the cross-section with the minimum area (usually near the middle of the vertebral body) Since it was difficult to visually determine where the minimum slice was located, two or three slices were taken around the minimum such that the smallest of those slices could be determined using further measurement tools. A scale line was drawn on each of the slices for further reference and the images were saved as JEPG files. It should be noted that one vertebral body (Spine 3, T2) was excluded from this reslice procedure as it was outside of the field of view during the initial CT scan and could
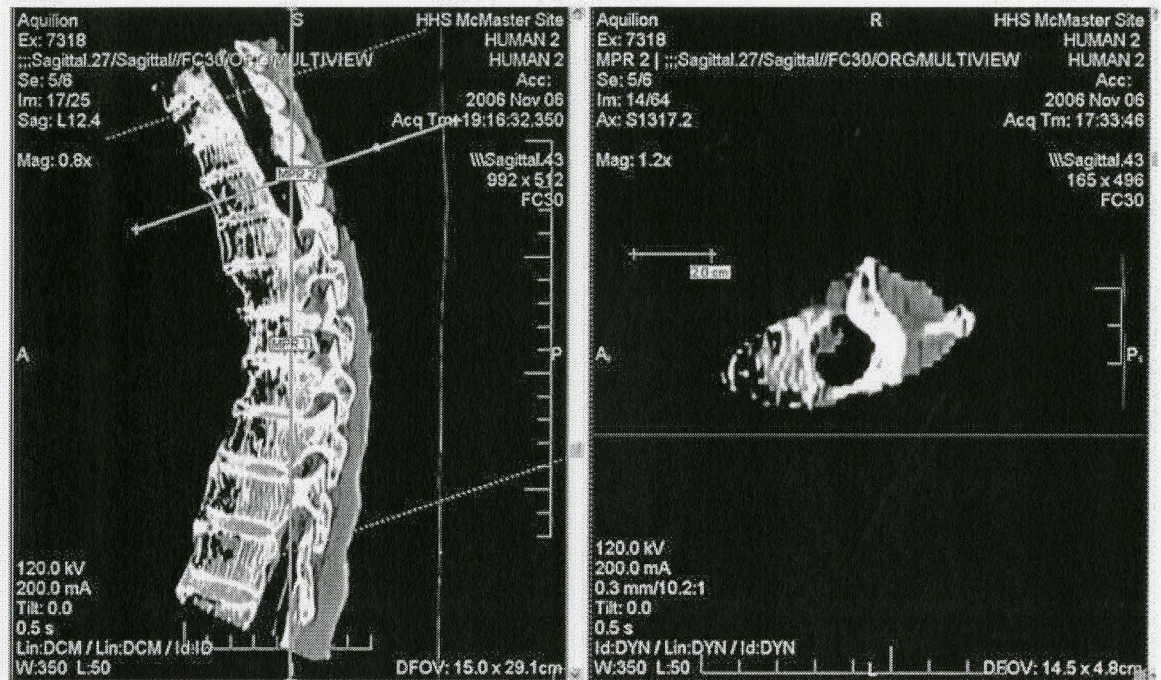
Figure 3.5: New slice location selection using MPR tool (left) and resulting slice (right)

not be accurately resliced using the MPR tool. For this reason, certain geometrical measurements could not be attained for this specimen.

### 3.3.2  Determination of Cross-Sectional Area

A Java-based image analysis program called Image J was used to determine the geometrical properties of each of the MPR slices (example of slice shown in Figure 3.6. Using the measurement line as a reference, the known length was entered under "set scale" in order to determine the number of pixels per millimeter in the image. A smoothing algorithm and a binary conversion were applied to the image. A rectangular sectioning tool was then used to select the vertebral body with the bottom

Using the drawing tool, any gaps in the edges of the vertebral body were manually filled in (Figure 3.8, left) and the rectangular selection was made in the same manner as the previous method. The "Analyse Particles" tool was once again used and produced the outline shown in Figure 3.8, right.



Figure 3.8: Rectangular selection of vertebral body (left) and region captured in area measurement technique 2 (right)

A paired t-test was performed which showed that there was no significant statistical difference between the area measurements attained using the two techniques. Therefore, for all further analyses, only the cross sectional area measurements attained using the first technique were used. For each MPR slice, the width and depth were also measured using the line tool in Image J and the scale line as a reference. The location of these measurements is shown for an example slice in Figure 3.9.
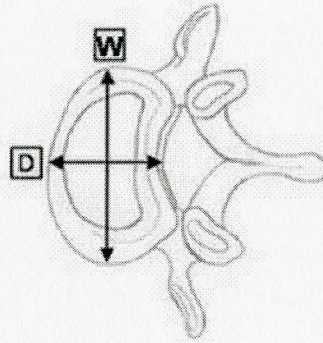
Figure 3.9: Slice width and depth measurement locations.

### 3.3.3  Height and Width Measurements

HCT images were prepared for geometric measurement using a volume visualization package called VolView  Using this software, the HCT slices were reconstructed into a 3D volume as shown in Figure 3.10 (right, sagittal view)  A close up view of the target vertebra of each functional unit was also captured. Using Image J once again, measurements of the height and width of the vertebra (VH and VW), top (TEH and TEW) and bottom endplates (BEH and BEW) were taken using the scale line in the image as a reference.  Figure 3.11 shows the location of each of the measurements. Each measurement was repeated three times and the average taken in order to attain a precise value.

Figure 3.10: Volume reconstruction of spine 4, left sagittal view
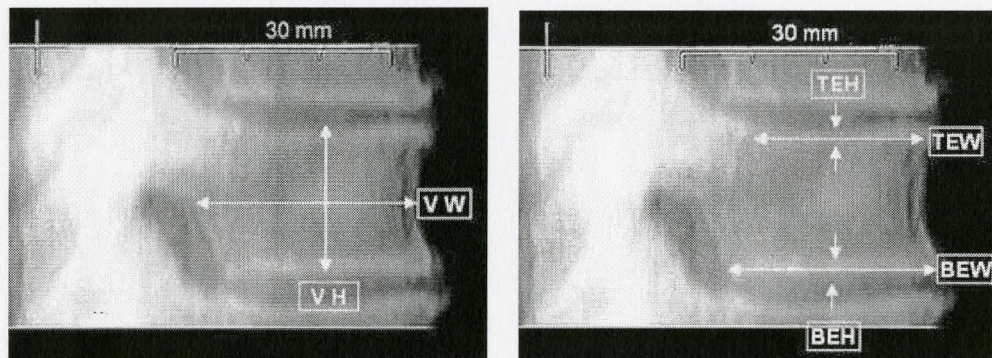


Figure 3.11  Measurements(a) Vertebral (b) Endplate.

## 3.3.4   Determination of AP concavity

Each of the MPR views was printed out and tangents were drawn at the location

of the minimum thickness of the anterior and posterior sides of vertebra extending to

the top and bottom endplates.  The height of the anterior (HA) and posterior (HP)
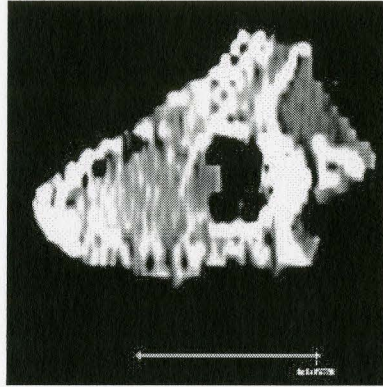
Figure 3.6: New slice created with MPR tool.

border selected as the top of the spinal canal. The "Analyse Particles" tool was used to count all of the black pixels in the selected region, which was then converted to a cross sectional area. This process is illustrated in Figure 3.7  Using this methodology, any holes in the vertebral body that extended through the edges were excluded from the cross sectional area.
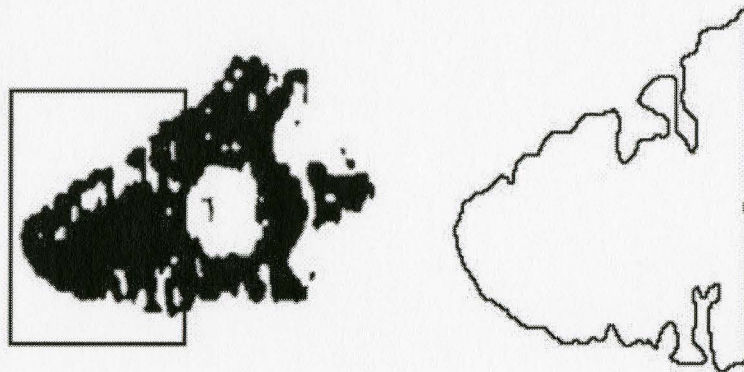


Figure 3.7  Rectangular selection of vertebral body (left) and region captured in area measurement (right)

A second calculation of the cross sectional area was found in order to determine the effect of including edge holes in the vertebral area. In this method, the scale was set as outlined above and the image was smoothed and a binary conversion applied.

tangents as shown in Figure 3.12 were manually measured using a ruler  The ratio of anterior to posterior height was then determined as a measure of the vertebral concavity in the AP direction.
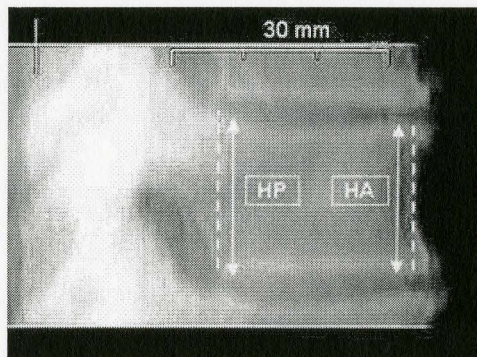


Figure 3.12: Tangent measurements.

## 3.4  Mechanical Testing

The effects of weight bearing and muscle action cause the vertebrae to experience many different loading configurations in daily life. For the purposes of this study, it was necessary to simplify the loading condition to uniaxial compression in order to create a standardized and precise testing methodology  This is the loading condition experienced most greatly by the vertebral body and its use allows for easy comparison with other studies found in the literature.

### 3.4.1  Preparation of Specimens

Each spine section was divided, while frozen, by transverse cuts through the midplane of every second vertebral body  This created "functional units" consisting of one full vertebral body, two intervertebral discs and half of the adjacent vertebral

bodies as shown in Figure 3.13. The specimens were once again sealed in polyethylene
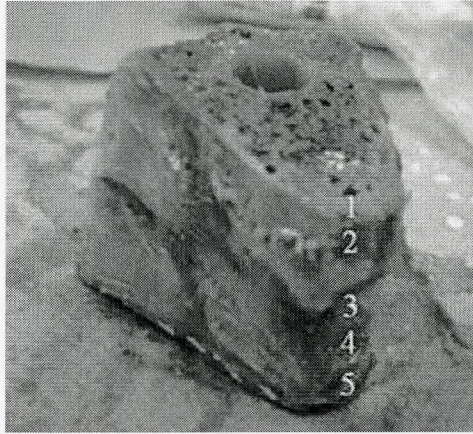


| Number | Description |
|--------|-------------|
| 1 | Proximal half vertebral body |
| 2 | Proximal intervertebral disc |
| 3 | Central vertebral body |
| 4 | Distal intervertebral disc |
| 5 | Distal half vertebral body |

Figure 3.13: A vertebral functional unit (left) and anatomical labeling chart (right)

bags using a commercial vacuum sealing device and returned to the freezer until they

were needed for testing. The functional units were thawed at room temperature for

3 hours and all soft tissue was removed by dissection. The thawed specimens were

stored in a refrigerator at 4°C for up to one day prior to mechanical testing.

### 3.4.2    Experimental Fixture

The fixture used for compression testing consisted of two aluminum cups which

contained the proximal and distal ends of the functional unit specimen. These cups

will hereafter be referred to as the proximal and distal cups. Screw holes were located

at the 12, 3, 6 and 9 o'clock positions, 0.25" from the top of the cup. During testing

screws could be threaded into the specimen at these locations in order to hold it in

place. A threaded adaptor was created such that the proximal cup could be threaded

directly to the load cell attachment during testing. A pin adaptor was created that

would rest inside a hole in the bottom of the distal cup. The bottom end of the pin adaptor fit into cylindrical block that rested on the base of the mechanical testing machine.

### 3.4.3   Experimental Set-up

A thorough layer of Vaseline was applied to the inside of the proximal cup in order to prevent the specimen from becoming stuck to the cup. One batch of polymethylmethacrylate (PMMA) was prepared by mixing 3 scoops of the polymer powder with 18 mL of the monomer liquid. The mixture was applied to the bottom of the metal cup and the proximal end of the functional unit was inserted such that the PMMA filled in any gaps or irregularities in the specimen surface in order to ensure equal load transfer from the fixture to the specimen. The specimen was oriented to be perpendicular to the plane of the metal cup. PMMA was then applied around the circumference of the proximal vertebra up to the vertebral body/disc interface but not covering the facet joints of the specimen. After the PMMA had cured and hardened for 15 minutes, screws were threaded through the cup into the PMMA in order to prevent sliding of the sample in the XY direction during testing.

The proximal metal cup was attached with an adaptor to the crosshead of the universal testing machine. The adaptor/distal cup assembly was placed on the base of the testing machine. The above procedure was then repeated for the distal end of the functional unit and resulted in the specimen being oriented perpendicularly

to the machine crosshead, thus creating a uniaxial compression testing condition as shown in Figure 3.14.



| Number | Description |
|--------|-------------|
| 1 | Data acquisition system |
| 2 | Load cell |
| 3 | Crosshead |
| 4 | Crosshead adaptor |
| 5 | Specimen fixture |
| 6 | Base adaptor |
| 7 | Specimen |
| 8 | Manual controls |
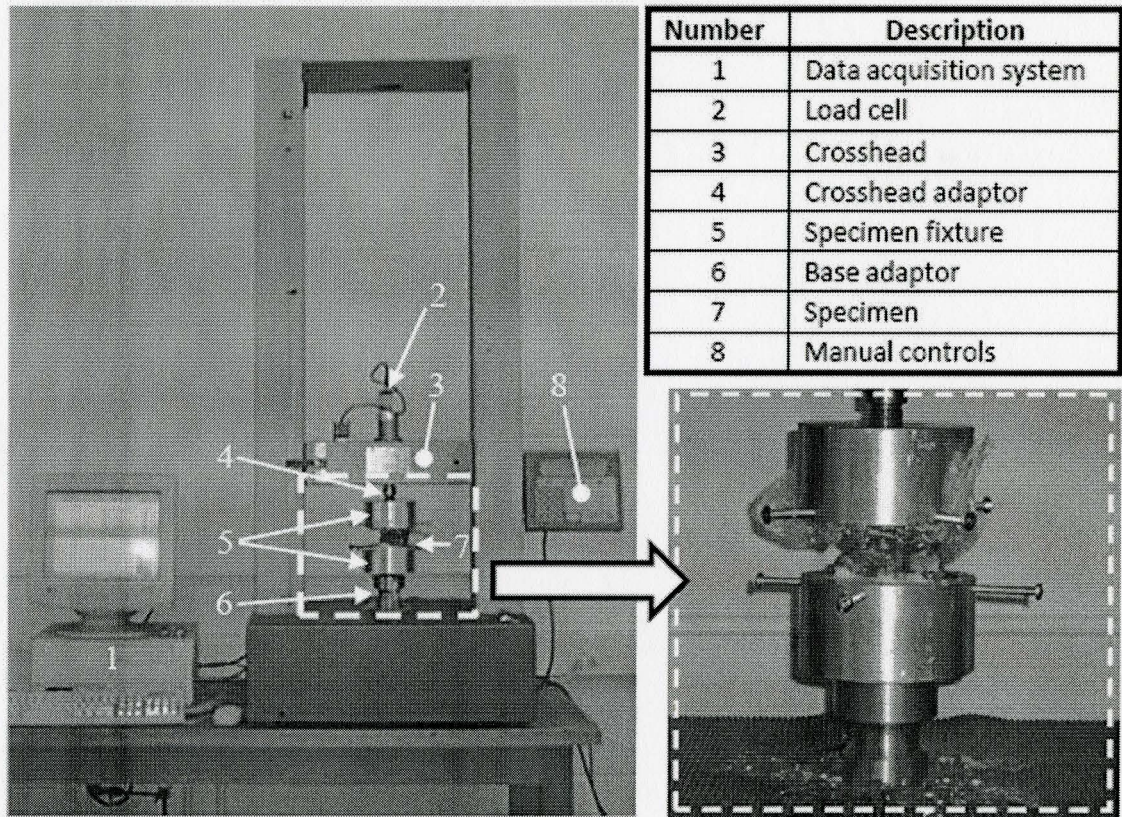
Figure 3.14. Experimental set-up (left) and description (right)

Figure 3.15 is a schematic of the experimental set-up illustrating how the specimen was held in place and uniaxial loading was ensured.

| Label Number | Description |
|---|---|
| 1 | Proximal fixture cup |
| 2 | Proximal vertebra |
| 3 | Target vertebra |
| 4 | Distal vertebra |
| 5 | Distal fixture cup |
| 6 | PMMA reinforcing vertebra, extending up to vertebral body/intervertebral disc juction |
| 7 | Screws driven into hardened PMMA to ensure no lateral motion during testing |
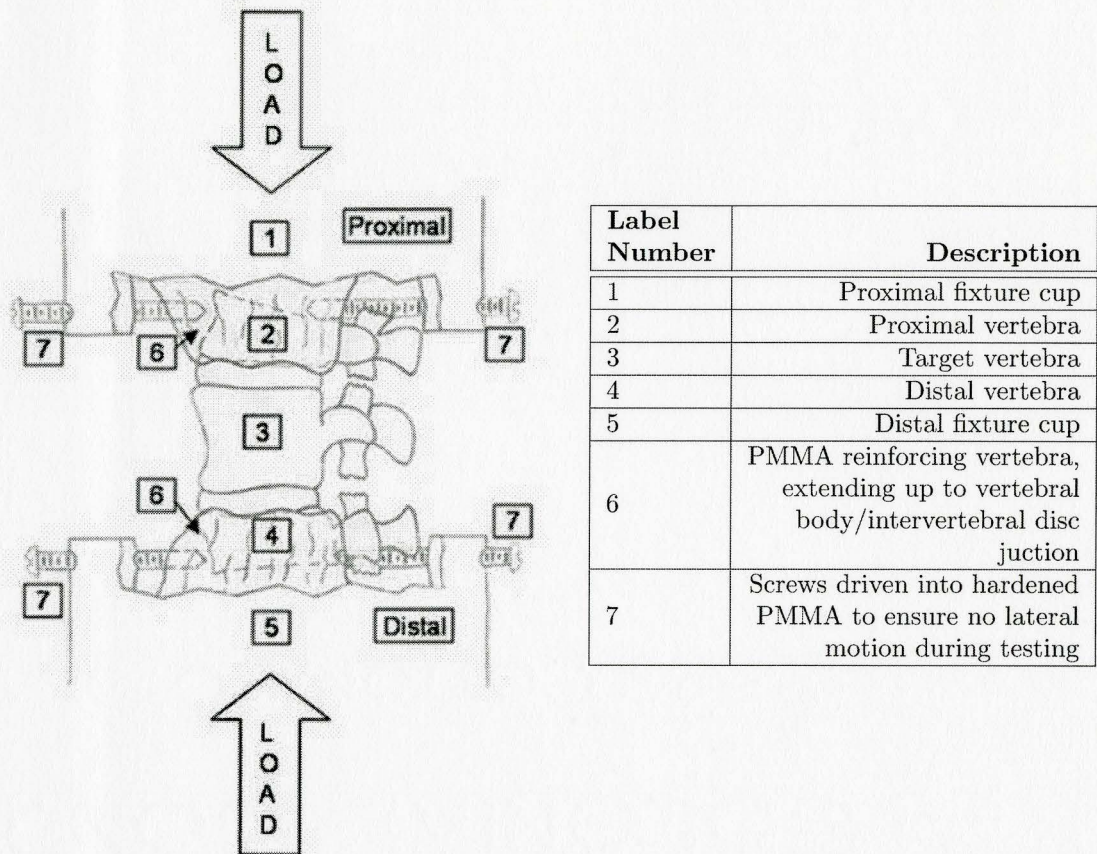
Figure 3.15: Schematic (left) and description (right) of functional unit compression test.

### 3.4.4   Mechanical Testing Procedure

Uniaxial compression tests were performed at room temperature on a Lloyd's screw-driven twin column testing machine. To verify the accuracy of the 30 kN load cell, the machine was calibrated using 10 lbs gauge weights as shown in Appendix II. A weight holder was attached to the load cell using an adaptor and the weights were added one at a time to a total of 150 lbf while the load was measured using Nexygen Ondio data acquisition software. The measured load was plotted versus the applied load and the line of best fit ($R^2 = 0.99998$) was taken for the plot. The

measurements were found to be accurate within about 3% with a precision of $\pm 2$ N

The specimens were thoroughly sprayed with a normal saline solution (0.9% sodium

chloride) in order to maintain hydration throughout mechanical testing. Prior to the

initiation of each test, the specimen was compressed to a deformation of 0.2 mm

(measured as the distance of the crosshead from the initial starting position) and

unloaded back to 0 mm deformation. This was repeated 3 times in order to seat the

specimen in the PMMA and ensure a level load application surface. Each specimen

was then compressed to failure at a deformation rate of 0.083 mm/s while the load

and deformation were recorded by data acquisition software. For each functional unit,

load versus deformation was plotted as shown in Figure 3.16.
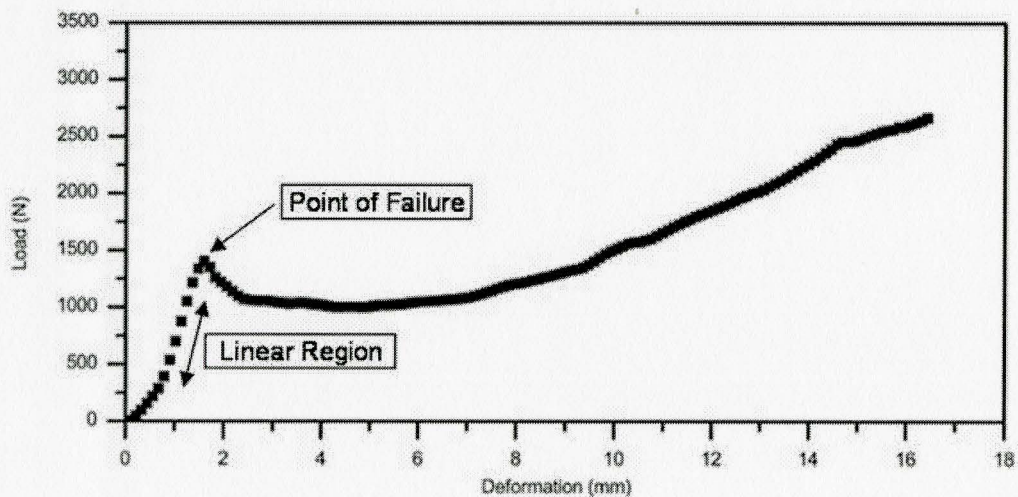


Figure 3.16: Example load versus deformation curve from compression test (Specimen 2T1-T3)

Failure load was defined as the first peak in the load-deformation curve after the
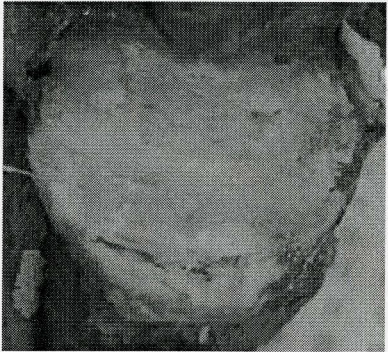
onset of plastic deformation but testing was allowed to continue until each specimen had undergone about 15 mm of deformation in order to ensure that fracture had indeed occurred. The stiffness for each functional unit was calculated as the slope of the linear region of the load-deformation curve.

### 3.4.5   Characterization of Intervertebral Discs

Following mechanical testing, the functional units were sectioned through the midline of the proximal and distal intervertebral discs such that the quality of the discs could be characterized. The discs were graded according to the Nachemson grading scale described in Krisner et al. [55] as shown in Table 3.2.

The majority of examined discs were moderately to severely degenerated with poorly distinguishable nuclei. A number of the specimens from spine 4 and 5 had visible osteophyte formation, which are bony growths characteristic of disc degeneration. A table containing the full details of the examination can be found in the Appendix III.

Table 3.2: Disc grading scale [55] and examples from current study.

| Grade | Description | Image example from current study |
|-------|-------------|----------------------------------|
| 1 | Discs without changes visible to the naked eye, gelatinous shiny nucleus, easily delimited from the annulus fibrosus, which is macroscopically free of ruptures | None in current specimen set |
| 2 | Discs with macroscopic changes in the nucleus pulposus, nucleus somewhat more fibrous, can be clearly distinguished from the annulus, which is intact |  |
| 3 | Discs with macroscopic changes in both the nucleus pulposus and the annulus fibrosus: nucleus more fibrotic, but still soft; boundary between nucleus and annulus not so distinct, but can still be seen |  |
| 4 | Discs exhibit fissure formation and cavities in both the nucleus and annulus; marginal osteophytes often found |  |

### 3.4.6   Helical Computed Tomography (Post-Test)

Following compression testing, each functional unit was imaged using computed tomography once again in order to characterize the fracture that occurred in each specimen. Scans were conducted using a single slice GE 120 CTI machine. The technologist used a bone algorithm with a slice thickness of 3 mm and a 1.5 mm interval. The pixel size was $\sim$ 2.5 mm and the field of view was 13x13 cm. The x-ray parameters were set to 200 kV and 160 mA.

## 3.5   Experimental Limitations

### 3.5.1   Factors Affecting Specimen Quality

The specimens attained for this study had been previously frozen for 5 years. The effect of frozen storage for this length of time is unknown and was a variable beyond the control of this study. A survey of the literature did show evidence that bone stored at -20°C for periods of up to 8 months showed very little change in its mechanical properties [15] and that the compressive properties of cancellous bone were unaffected by five freeze thaw cycles [56] Additionally, due to the small number of samples available for the study, features that were present tended to be overrepresented. For instance, there were osteophytes present on several of the intervertebral discs of the functional units from spine 4 and 5. This means that the effect of osteophyte formation will be very influential in this set of results, while the effect may be less in a greater sample size.

### 3.5.2   Imaging

Imaging of the specimens was conducted while frozen in order to minimize the number of freeze-thaw cycles. This may raise the concern that the measurement of bone density would be affected by the sample's frozen state. Evidence from the literature suggests that freezing does not significantly affect density measurements using pQCT [3] and it is a reasonable to make the assumption that the DXA results would not be significantly affected either. It should be kept in mind that freezing may affect images attained using MRI since ice formation causes a redistribution of water in the specimen resulting in an altered signal. The acquisition of helical computed tomography images was conducted on machines that are in current clinical use at Hamilton Health Sciences Center. This resulted in very limiting time constraints being placed on the use of the machines and necessitated images being taken as quickly as possible. In order to accomplish this, the resolution of the images was reduced, therefore reducing the scan time. Also, the computer equipment available for visualization of the images had limited memory and computing power. The combination of these factors resulted in sub-optimal images that limited the type of geometrical measurements that could be subsequently made.

### 3.5.3   Mechanical Testing

The greatest obstacle faced in effective compression testing of the functional units was the correct placement of the specimen in the fixture in order to ensure

uniaxial loading. In preliminary tests on ovine specimens, many different approaches to create the proper loading condition were explored. A "worst case" scenario was examined in which a lamb spine specimen that was much taller than any of the human specimens was tested to ensure the sample would not fail in bending rather than compression. Proper application of the PMMA on ovine specimens was practiced such that a level load bearing surface was created on each end of the specimen. Examination of the human specimens showed that the curvature of the individual functional units was minimal and that the assumption of uxiaxial loading could be made. Some researchers choose to conduct mechanical testing of bone under simulated *in vivo* conditions [4, 8] Several studies described in Turner and Burr [17], indicated that testing bone specimens at 23 °C increased Young's modulus by 2-4%. None of studies indicated the effect of temperature on failure load. For the purposes of this study, this minimal variation was deemed acceptable.

### 3.5.4   Geometric Measurements

A significant amount of subjectivity was present in the technique used to make geometrical measurements of the vertebrae. To make the measurements in a timely fashion, the location of the region to be measured, including the points where the measurement began and ended, had to be determined visually and would likely vary from one investigator to the next. In order to provide a more precise value, each measurement was taken 3 times and the average calculated.

# CHAPTER 4
# Results and Discussion

The overall objective of this thesis work was to identify factors other than established parameters such as bone density to explain the variation in bone strength. Towards this goal, material and geometric properties of vertebrae were assessed using imaging techniques and analyses. The strength of vertebrae was determined by conducting compression tests on vertebral functional units. In this chapter, the amalgamation of this data into mathematical expressions that describe failure load and stress at failure will be addressed. Additionally, this study presented the opportunity to clarify the controversial association between bone mineral density and bone strength that has persisted in the literature [4–8, 10]. In order to accomplish these objectives, the following methodology was employed:

- The failure characteristics of the functional units were investigated and related to the trends found in other studies elsewhere.

- The clinical measurement currently used to diagnosis osteoporosis (aBMD) was related to bone strength and compared to other findings in the literature. The discussion of density was extended to include measures of total density and trabecular density attained using pQCT.

- The measured parameters were analysed using projection to latent structures and multiple linear regression techniques, producing expressions that describe the key factors that contribute to vertebral failure load and stress at failure.

## 4.1  Failure of the Functional Units

Each of the functional units was examined after mechanical testing for evidence of failure. HCT imaging showed that the failure occurred in the target vertebrae of each functional unit as was intended. Generally, wedge or crush fractures were observed in each of the target vertebrae with cracks extending through the cortical shell. Further description of the failure characteristics for each functional unit can be found in Appendix IV

### 4.1.1  Load at Failure

Measured failure loads were reported for the target vertebra in each functional unit. The plot of load versus vertebral location shown in Figure 4.1 indicates that the failure load was significantly lower (under 2500 N) for spines 1, 2 and 3 which corresponded to the female patients. This was an expected finding as it has been shown that men typically have bigger vertebrae than women, allowing them to endure a greater load [57] The failure load for spine 5, vertebra T11 appears to be an outlier on the plot. Examination of the intervertebral discs for this functional unit showed an osteophyte on the distal disc bridging from T11 to T12 as shown in Figure 4.2,
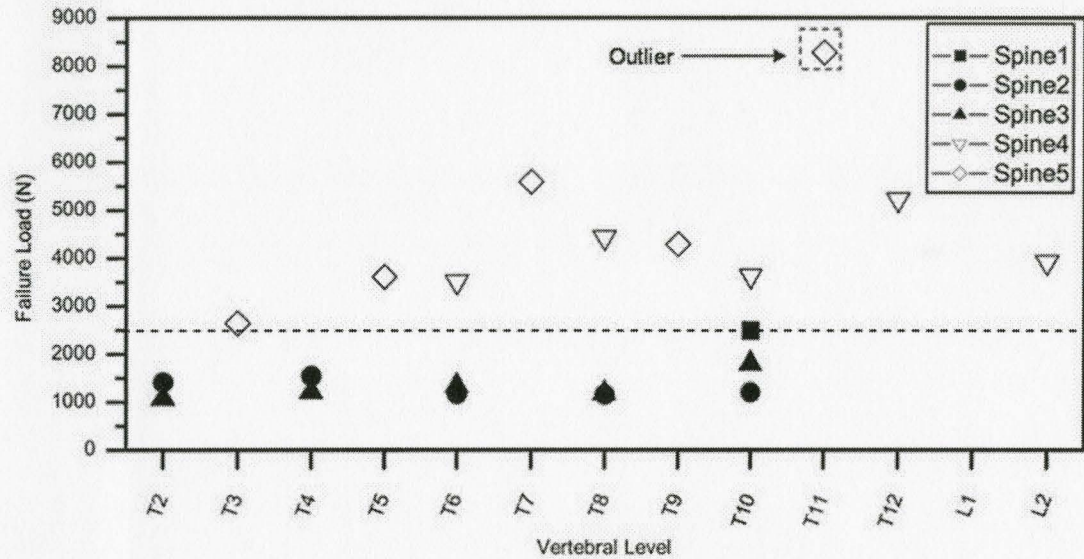
Figure 4.1. Plot of failure load versus vertebral level.

(left)  Figure 4.2, (right) shows a cross-sectional view of the disc with the osteophyte clearly present on the anterior region of the disc. The osteophyte has fused the disc, possibly altering its load transferring properties. This may have increased the ability of this functional unit to resist compressive loading. This study generally did not



Figure 4.2: Left sagittal view of spine 5, T11 (left) and cross-sectional view (right)

show the trend that failure load increases in the caudal direction as was reported in

the literature [1]. This may be due to the relatively low number of samples used in

this study. While 21 functional units were investigated in the current study, these

were derived from only 5 donor spines. The study by Brinckmann et al. utilized a

greater number of samples, with 53 donor spines included.

### 4.1.2  Stress at Failure

It is often more practical to evaluate normalized characteristics in order to
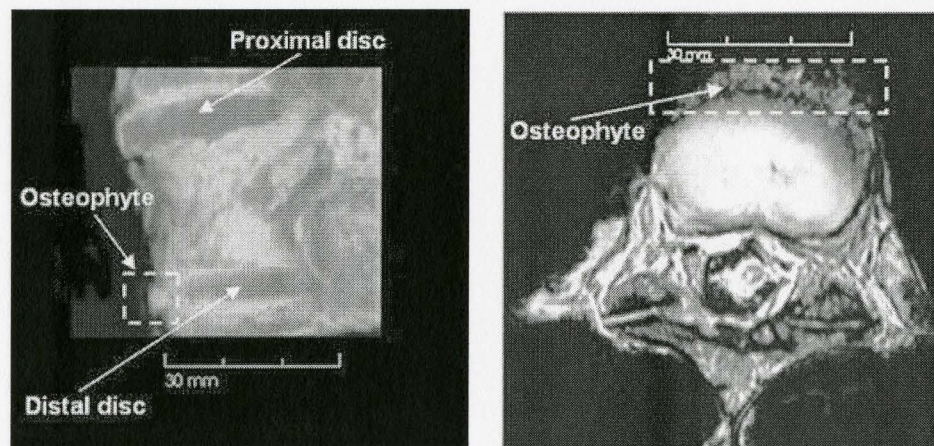
account for sample variability and to facilitate easy comparison between studies.

Here, the effect of specimen size was reduced by calculation of the stress at failure,

defined as:

$$\sigma = F/A \tag{4.1}$$

where:

- F is the load at failure

- A is the cross-sectional area of the top endplate

The top endplate area was selected for inclusion in the stress calculation because

it has been shown that that the typical fracture mechanism experienced by a vertebra

compressed uniaxially is an endplate fracture. This occurs as the strain limit of the

trabecular bone bordering the endplate is exceeded by the intrusion of disc material

into the trabecular region [1]. In the current study, it was observed that failure

initiated and/or propagated in this region in many of the specimens, therefore the

magnitude of stress at this location was of interest.

### 4.1.3   Note on Intervertebral Discs

The intervertebral discs were graded as described in Table 3.2 with the details

being presented in Appendix III. It was observed that osteophytes were present on

several of the discs, particularly in the specimens from male donors.   Comparison

of the failure characteristics for specimens with and without osteophytes showed no

clear trend.  The grade assigned to the proximal and distal disc for each functional

unit was related to failure load and to stress at failure.  Since the nature of the

relationship between the disc condition and the failure load was unknown, several

different data fitting techniques were used to interrogate the data.  There was no

significant correlation (all $R^2 < 0.13$) with failure load or with stress at failure for

either proximal or distal discs using linear, logarithmic, power or exponential data

fitting techniques.

## 4.2   Correlations with Density Measurements

The current technique for diagnosing osteoporosis is based solely on the premise

that denser bones are less likely to break.  In this study, this idea was investigated

by relating bone density to the failure load measured when vertebral functional units

were uniaxially compressed.  Figure 4.3 shows the relationship between failure load

and density measured using both DXA and pQCT.
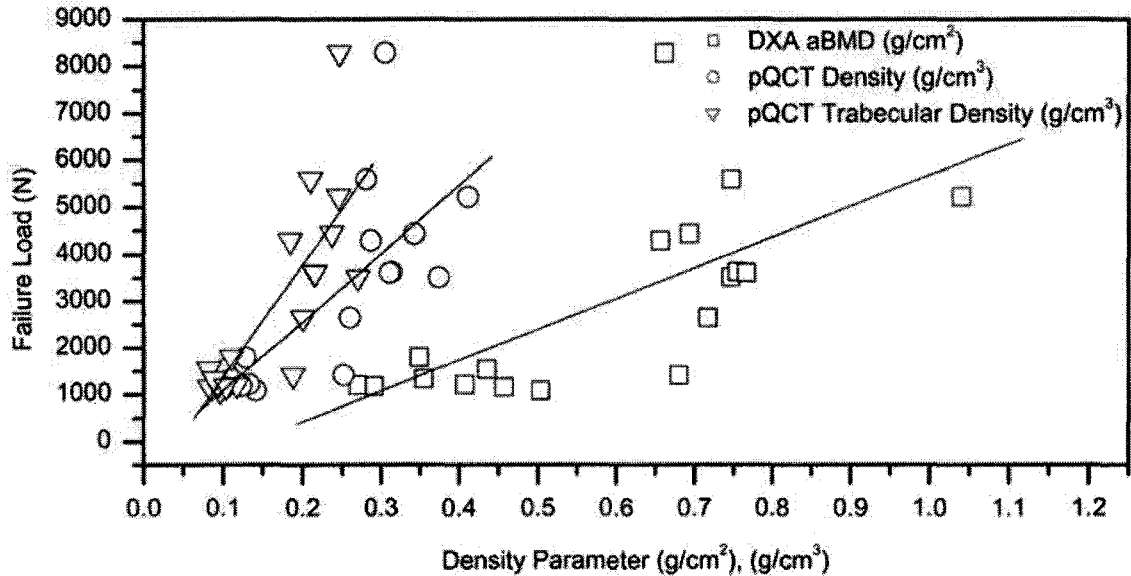


Figure 4.3: Plot of failure load versus various bone density measurements.

Three measurements were excluded from this plot as the pQCT density values could not be determined using the area measurement algorithm (due to unclear slice edges). For comparison with the results of previous studies, linear regression was applied and an $R^2$ value of 0.458 (P = 0.002) was found for the correlation between failure load and DXA aBMD. This correlation was improved by plotting failure load versus slice 2 pQCT total density ($R^2 = 0.575$, P = 0.0003). The relationship between failure load and slice 2 pQCT trabecular density yielded the strongest correlation of the densities measured ($R^2 = 0.631$, P < 0.0001). The correlation between DXA aBMD and failure load was typical of the values found in the literature [7, 10] but the correlation between pQCT trabecular density and failure load was stronger than

those found in other studies. The values for $R^2$ given in the literature range widely

from 0.08 [8] to 0.50 [5]  The study with the lowest correlation (Singer et al.) was re-

examined and it was observed that the donors in this investigation ranged in age from

29-89 with a mean age of 66. This wide age range introduced a lot more variability

into the correlation between failure load and vertebral trabecular density (VTD) as

shown in Figure 4.4, an excerpt from Singer et al. [8]  The plot indicates that some
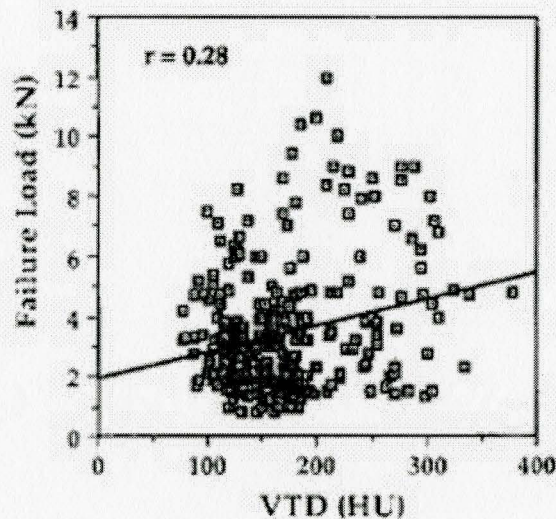


Figure 4.4: Excerpt from Singer et al. [8]

of the specimens had failure loads in excess of 8000 N (the maximum found in the

current study)  This corresponded to more widely spread data and therefore a lower

coefficient of determination. The use of a linear fit is also questionable in this case, as

the data appeared not to be correlated. These results illustrate the crucial nature of

selecting the correct age range of donors when designing a study to look at properties

of trabecular bone. Since trabecular bone undergoes significant degradation with ag-

ing, particularly a reduction in the thickness and number of trabeculae [58], including specimens from such a wide age range could undermine the integrity of the data. The current study involved donors with a much smaller age range (60 - 87 years), which meant that the specimens had likely undergone a similar amount of degradation, particularly when grouped by gender. This may be the reason for the strong correlation found between trabecular density and failure load found in this study. It was noted that data presented in Figure 4.3 may be better fit using a non-linear relationship. Exponential curve fitting was applied and the $R^2$ value for the correlation between DXA aBMD and failure load was found to be 0.6. The correlation was even stronger between pQCT density measurements and failure load with $R^2$ values of 0.73 and 0.76 being calculated for total and trabecular density respectively. The exponentially fit plot is shown in Figure 4.5. This appears to be the first time this particular type of relationship between load and density has been reported, and warrants corroboration by further study. If this relationship holds, it may indicate that small increases in bone density greatly increase the load that a vertebra can endure before failure.
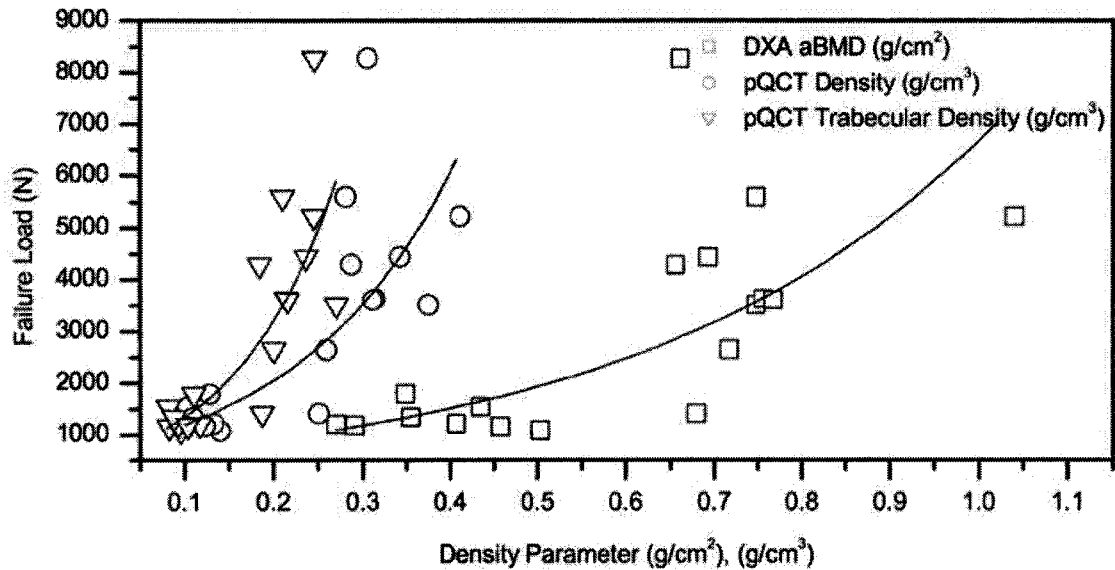
Figure 4.5: Failure load versus various bone density measurements fit with an exponential curve.

The correlation between density and stress at failure was also investigated as shown in Figure 4.6. The correlations found between measurements of density and stress at failure were only slightly lower than those found for failure load. $R^2$ values for DXA aBMD, pQCT total density and pQCT trabecular density were 0.347 (P = 0.002), 0.515 (P = 0.0002) and 0.566 (P < 0.0001) respectively. The correlation between DXA aBMD and stress was within the range presented in the literature ($R^2$ = 0.16 - 0.61) [4, 5, 10]. Only one other study investigated the correlation between total density measured by pQCT and failure stress. This work, by Ebbessen et al. [3] found an $R^2$ value of 0.86. This is significantly higher than the value found in the current study possibly due to the experimental approach taken by Ebbessen et al. which included testing only individual vertebrae in compression with no interface between
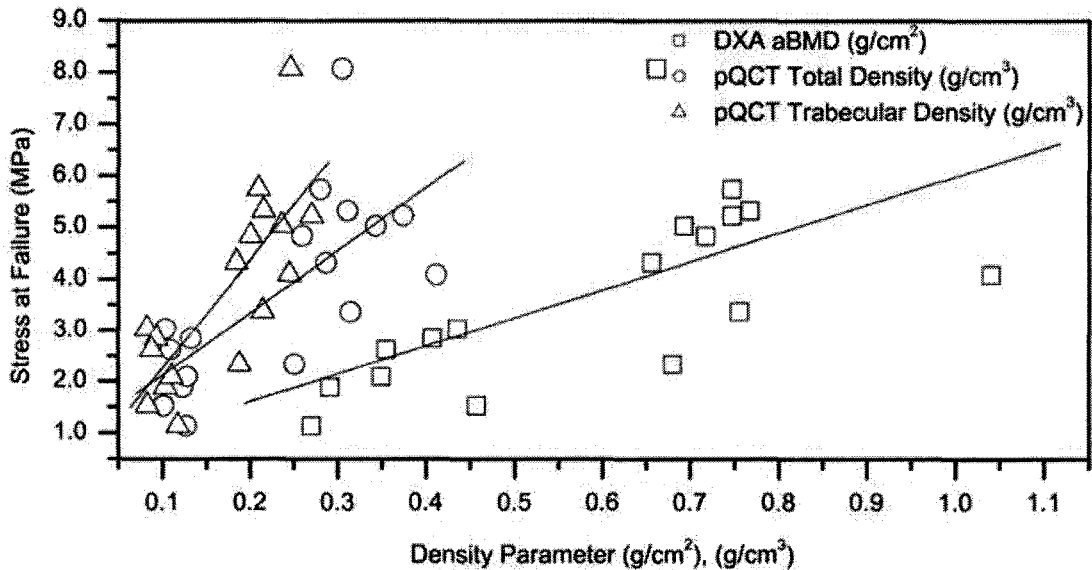
Figure 4.6: Stress at failure versus density measurements.

the specimen and the loading platen. Finally, the correlation between trabecular density and failure stress found in the current study was compared to the values found in the literature. The current $R^2$ value of 0.566 was within the range of the values found in the literature ($R^2 = 0.36$ - $0.62$) [4, 5, 8, 10]. While it has been demonstrated that there are significant positive correlations between density and failure load as well as between density and failure stress, there still remains at least 25% of the variance in these strength parameters that is not explained by these simple linear regression models. The incorporation of relevant geometrical parameters into the model might improve the explanation of vertebral strength, as detailed in the following.

## 4.3    Effect of Cross-Sectional Area on Explanation of Failure Load

Studies by Brinckmann et al. [1] and Singer et al. [8] indicated that the explanation of failure load could be improved for trabecular density by multiplying this density by endplate area or mid-body area. This finding was investigated for the current set of results. As shown in Figure 4.7, this addition of cross-sectional area into the model significantly improves the fit of the correlation.



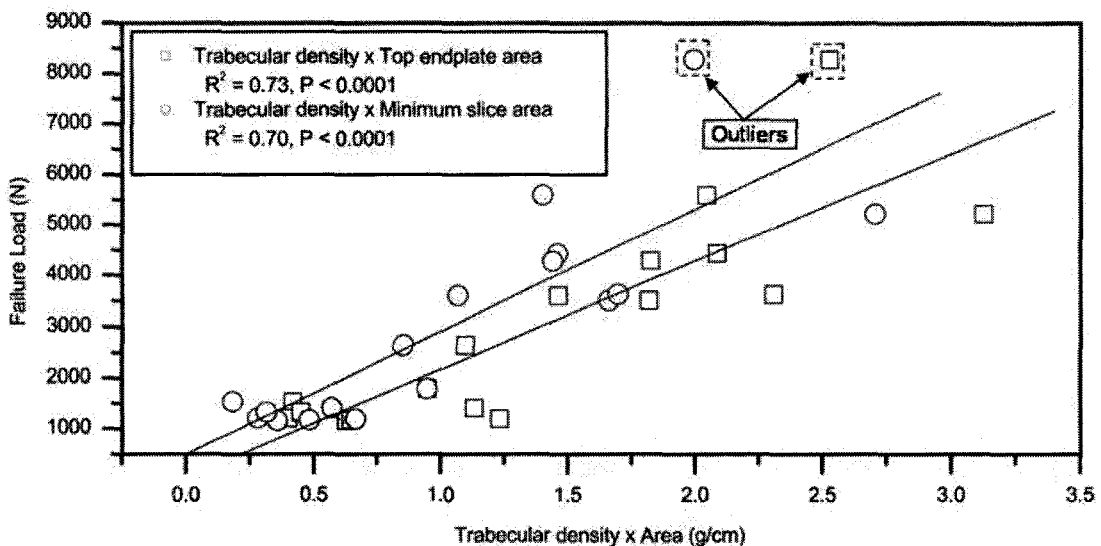Figure 4.7: Failure load versus trabecular density multiplied by area.

Upon reexamining the original dataset, it was observed that the variability in density measurements was far less than in the cross-sectional area measurements. Therefore, this new parameter partially incorporates the effect of vertebral size into the model, which has been shown to be highly influential in terms of the amount

of load the specimen can withstand before failure. This finding demonstrated the improvement that incorporating a single geometric variable could provide to the explanation of failure load and provided the impetus behind investigating the effect of other geometric parameters. In summary, how much of the 25% unexplained variance could be accounted for by the inclusion of measures of vertebral geometry?

## 4.4   Multiple Linear Regression

In order to determine the combination of parameters that best explain bone strength, it was necessary to conduct multiple regression analysis. As the nature of this study was preliminary, it was desirable to conduct a simple statistical analysis. Additionally, the true nature of the data fit was unknown so the multiple regression technique used was restricted to first order, linear regression.

### 4.4.1   Data Preparation

Due to the large number of geometric parameters measured in this study, data sorting was required in order to create a concise and useful model. Additionally, due to difficulties with the measurement techniques, there was approximately 5% missing data in the set which complicated the analysis process. Since linear regression assumes that all the variables are independent and that there is no missing data, it was necessary to pre-screen the data before conducting linear regression.

### 4.4.1.1   Projection to latent structures

Data sorting was accomplished using a statistical software package called SIMCA

P+ 11. An analysis technique called projection to latent structures by mean of partial

least squares (PLS) was conducted on the raw data in order to determine which vari-

ables were of greatest importance to the explanation of failure load as well as stress

at failure. PLS is a very effective tool for dealing with noisy, collinear and incomplete

data sets. In this technique, the Y matrix (the dependent variable) is described as

relating linearly to a function of the X matrix (the predictor variables) and a residual

matrix (E) by an equation of the form:

$$Y = f(X) + E \qquad (4.2)$$

PLS creates a projection of both the X and Y spaces on low dimensional hyper

planes while maximizing the correlation between the X and Y matrices. This is

accomplished by first centering and scaling the variables so that each one is treated

as equally important in the model. Each of the X and Y variables correspond to a

co-ordinate axis in a multidimensional coordinate system. In this thesis work, only

one Y variable was evaluated in each model so that Y space was represented by a

vector. Each row in the original dataset corresponds to two points, one in the X

space and one in the Y space, creating two data swarms. An example involving 3 X

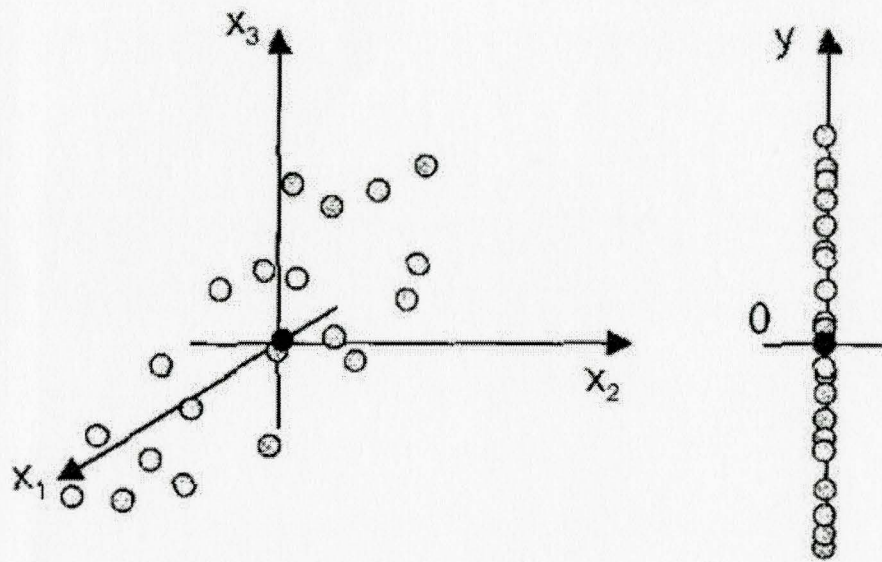variables and a single Y variable is shown in Figure 4.8.

Figure 4.8: Graphic representation of PLS technique [59]

Each point in the point swarm is projected onto a vector (called a component) that represents the X point swarm well and simultaneously correlates well with the Y vector  The co-ordinate of the each projected point is called the score, denoted by t. The distance from the original point in the swarm to its projected location on the component vector is called a residual. If the data has been well explained by the component vector, the residuals are small.  In order to improve the explanation of the data, a second component vector can be created which is orthogonal to the first. This component is situated such that it improves the description of the X swarm while correlating well with the Y residuals. Together, the first and second components form a plane. This process continues until the residuals are minimized. The mathematical basis of this PLS is Non-Iterative Partial Least Squares (NIPALS), the details of

which are outside the scope of this thesis. For more information on NIPALS, the reader is referred to Multi- and Megavariable Data Analysis by Eriksson et al. [59].

### 4.4.1.2   Variable importance in the projection

From the results of the PLS analysis, a "variable importance in the projection" plot (VIP) was created to illustrate which variables were most vital in the explanation of the Y variable. VIP is a weighted sum of squares of the PLS weight matrix, accounting for the amount of explained Y-variance in each dimension. The PLS weight matrix describes how the X variables are linearly combined to form the score vector, t. The VIP for a given variable, k, is described by equation:

$$VIP_{A,k} = \sqrt{\left( \sum_{a=1}^{A} SSR_a w_{ak}^2 \right)} \tag{4.3}$$

where:

- $w_{ak}$ is the weight matrix

- SSR is the squared sum of residuals

The VIP value indicates the relative influence of each X variable on the Y variable and allows X variables to be compared to each other. It should be noted that the squared sum of the VIP values equals the number of X variables in the model and that terms with a VIP value greater than 1 are most influential in the explanation of the Y variable.

### 4.4.1.3   VIP for geometric parameters and failure load

A PLS model was constructed with failure load as the Y variable and 23 geometric parameters (as shown in Table 4.1) as the X variables. From the PLS model,

Table 4.1: Geometric parameters included in PLS model.

| Region/Type | Parameter |
|---|---|
| Vertebral body | Height at midline<br>Width at midline<br>Anterior height<br>Posterior height |
| Top Endplate | Width<br>Height<br>Cross-sectional area<br>Cross-sectional width<br>Cross-sectional depth |
| Bottom Endplate | Cross-sectional area<br>Cross-sectional width<br>Cross-sectional depth |
| Minimum Slice | Cross-sectional area<br>Cross-sectional width<br>Cross-sectional depth |
| pQCT | Trabecular area (slice 1)<br>Trabecular area (slice 2)<br>Cortical area (slice 1)<br>Cortical area (slice 2) |
| Calculated | AP concavity (anterior height/posterior height)<br>Cortex concavity (average endplate area/minimum slice area)<br>Volume parameter (vertebral body height X minimum slice area)<br>Aspect ratio (vertebral body height/minimum slice area) |

a VIP plot was constructed to illustrate which geometric parameters most strongly related to failure load. A second PLS model was created relating the same geometric properties to stress at failure. The VIP plots that were constructed from both PLS models are shown in Figures 4.9 and 4.10.

It should be noted that the VIP plots do not distinguish between highly cor-
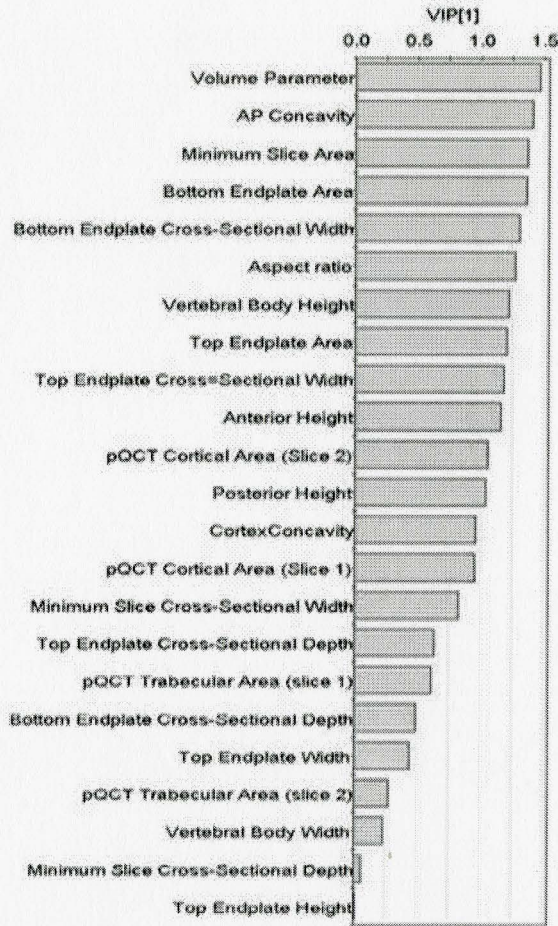
Figure 4.9: VIP plot of geometric parameters related to failure load.

related variables, meaning that two variables that are highly correlated could both have a high VIP value. In order to sort out correlations between these variables, a PCA analysis was conducted on all of the variables and the loading plot was examined. The VIP plot for failure load shown in Figure 4.9 indicated 12 variables with VIP values greater than 1  The loading plot showed that 3 of these; minimum slice area, top endplate area and bottom endplate area were all highly correlated. This was corroborated by simple linear regression between each combination of the three
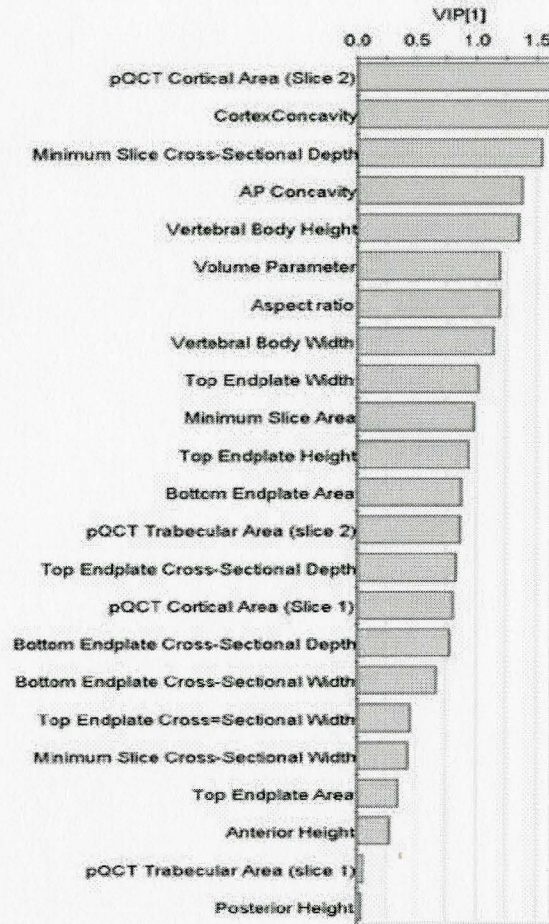
VIP[1]

| | 0.0 | 0.5 | 1.0 | 1.5 |

pQCT Cortical Area (Slice 2)
CortexConcavity
Minimum Slice Cross-Sectional Depth
AP Concavity
Vertebral Body Height
Volume Parameter
Aspect ratio
Vertebral Body Width
Top Endplate Width
Minimum Slice Area
Top Endplate Height
Bottom Endplate Area
pQCT Trabecular Area (slice 2)
Top Endplate Cross-Sectional Depth
pQCT Cortical Area (Slice 1)
Bottom Endplate Cross-Sectional Depth
Bottom Endplate Cross-Sectional Width
Top Endplate Cross=Sectional Width
Minimum Slice Cross-Sectional Width
Top Endplate Area
Anterior Height
pQCT Trabecular Area (slice 1)
Posterior Height

Figure 4.10: VIP plot of geometric parameters related to failure stress.

area measurements, each resulting in a plot with an $R^2$ value $> 0.85$. Each of the

area measurements was plotted against failure load and the one with the strongest

correlation (minimum slice area) was selected for inclusion in further modeling. The

VIP plot created for stress indicated 10 variables with VIP values greater than 1

The PCA loading plot indicated that there may be a correlation between the volume

parameter and the cross-sectional width of the minimum slice. This was verified by

performing simple linear regression on the two variables, then on each of the vari-

ables versus stress at failure. It was determined that the volume parameter was more

closely correlated with stress at failure so it was selected for use in further modeling.

### 4.4.2  Multiple Linear Regression - Failure Load Model

First-order multiple linear regression relates a single Y variable to k number of

X variables by an expression with the form:

$$Y = \beta_o + \beta_1 x_{i,1} + ... + \beta_k x_{i,k} + \varepsilon_i \qquad (4.4)$$

where:

- Y is the response variable

- $\beta_o$ is the population intercept

- $\beta_1$ through $\beta_k$ are the population coefficients

- $\varepsilon_i$ is the random error

A multiple linear regression model was formulated using a software package

called XLSTAT 2007. The model was created using the variables deemed most influ-

ential by VIP, with the addition of DXA aBMD. The results of the linear regression

model indicated that several of the variables were not very significant. All of the

variables with significance of P > 0.2 were removed from the dataset and a refined

model was created. This model was well fit by the X variables ($R^2 = 0.725$) and had a

strong significance value (P = 0.001). Details of the refined model are given in Table

4.2:

Table 4.2: Details of refined failure load model.

| Variable Name | Symbol | Coefficient Value | P Value |
|---|---|---|---|
| Intercept | | -3316.185 | 0.027 |
| DXA aBMD | aBMD | 7298.468 | 0.008 |
| Volume | V | 0.255 | 0.004 |
| pQCT Cortical area (Slice 2) | CA | -32.726 | 0.085 |

Simplifying the coefficients determined by the model, the failure load can be

expressed as:

$$\text{Failure Load} = 28621\text{aBMD}(\text{g/cm}^2) + V(\text{mm}^3) - 128\text{CA}(\text{mm}^2) - 13005 \qquad (4.5)$$

This result demonstrates that while failure load is dominated by aBMD, the

incorporation of volume and cortical area into the model increased the explanation

of failure load by nearly 30%. The positive correlation between volume and load

indicates that a vertebral body that has a larger overall size will be able to with-

stand higher loads. This parameter shows that recognizing the vertebra as a three-

dimensional structure rather than a two-dimensional area increases the explanation

of failure load. The negative correlation between cortical area and failure load is

an unexpected finding. Typically, an increase in the amount of cortical bone allows

the vertebra to resist a higher load. Reexamination of the original dataset showed

that the measurements of cortical area varied substantially. This may be due to the

presence of osteophytes on some of the specimens that may have been indistinguishable from cortical shell, skewing the area measurements. Further study involving a larger number of specimens is warranted in order to clarify this result. Although the correlation with load was improved when aBMD was replaced with pQCT density measures (trabecular density and total density) in the simple linear regression case (previously illustrated in Figure 4.3), the same trend was not observed for the multiple regression model. Using the refined model, aBMD was first replaced with pQCT trabecular density (slice 2), then with pQCT total density (slice 2). The resultant models showed no significant improvement over the aBMD model ($R^2 = 0.745$ and 0.721 respectively).

### 4.4.3   Multiple Linear Regression Model - Stress at Failure Model

The same approach was applied to create a model for stress at failure. The 10 variables determined to be significant with VIP plus aBMD were correlated with stress at failure. Once again, there were several parameters that were insignificant in the multiple linear regression model. All parameters with significance of $P > 0.2$ were removed and the model was refined. The resulting model had a very good fit ($R^2 = 0.871$) and significance ($P < 0.0001$). The details of the model are shown in Table 4.3.

This model allows the relationship between stress at failure and the X variables to be described as:

Table 4.3: Details of the refined stress at failure model.

| Variable Name | Symbol | Coefficient Value | P Value |
|---|---|---|---|
| Intercept | | -2475714 | 0.365 |
| DXA aBMD | aBMD | 3784075 | 0.058 |
| Vertebral body height | H | 782416 | < 0.0001 |
| pQCT Cortical area (Slice 2) | CA | -21889 | 0.053 |
| Cortex concavity | CC | -1669480 | 0.022 |
| Minimum cross section depth | MD | -305168 | 0.001 |

$$\text{Stress at Failure} = 173\text{aBMD}(\text{g/cm}^2) - 76\text{CC} + 36\text{H}(\text{mm}) - 14\text{MD}(\text{mm}) - \text{CA}(\text{mm}^2) + 113 \quad (4.6)$$

In this model, the cortex concavity emerged as a geometric variable that greatly influences stress. The cortex concavity was calculated as the ratio of the average endplate area to the minimum slice area. This parameter described the severity of the cortex curvature on the vertebral body. The model results indicated that cortex concavity had a negative, linear correlation with stress at failure. This indicated that as the cortex concavity increased, the amount of stress that can be tolerated by the specimen is reduced. Additionally, the height of the vertebra emerged as an important parameter in this multi-variable model. The linear relationship between vertebral height and stress at failure was also investigated and found to have coefficient of determination of 0.23, indicating that even on its own, height has a relationship with stress at failure. The reason for the significance of height in this model remains unknown at this time. It is possible that this result was a coincidence due to the

low number of specimens utilized in this study  Further investigation with a larger

number of samples is necessary in order to clarify this result. A VIP plot, shown in

Figure 4.11, of the correlation between different measures of bone density and stress

at failure indicated that there were 3 measures of density acquired with pQCT that

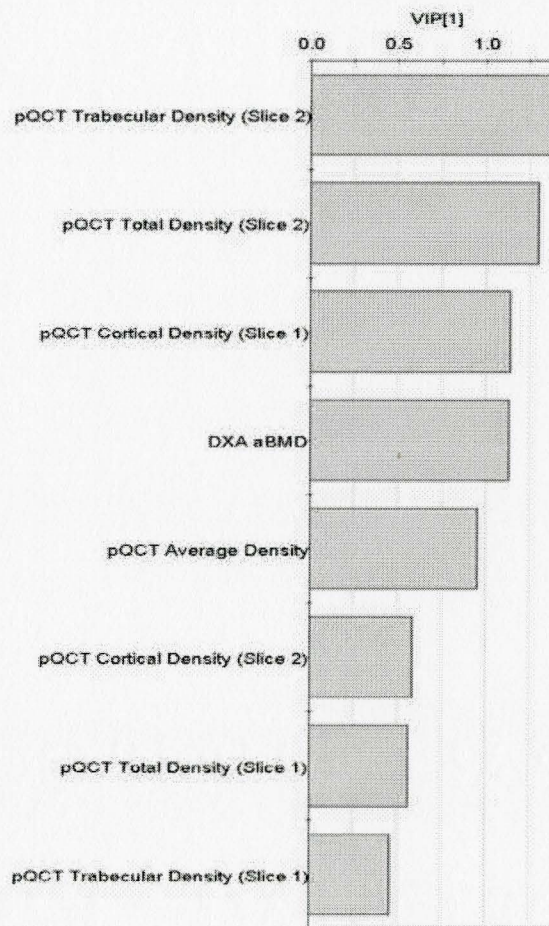were more closely correlated with stress at failure than aBMD



Figure 4.11  VIP plot of density parameters related to stress at failure.

The model described in Table 4.3 was run again, replacing aBMD with pQCT

trabecular density (slice 2), pQCT total density (slice 2) and pQCT cortical density

(slice 1). A minor improvement in the correlation was observed for each of these subsequent models ($R^2$ = 0.887, 0.885, 0.901) but the change was so slight that it cannot be concluded whether it is the type of density being measured that is changing the correlation or simply the variability of the specimens.

# CHAPTER 5
# Conclusions and Future Work

## 5.1   Conclusions

This study served as a preliminary investigation into the factors, other than density, that affect the strength of human vertebrae. Through medical imaging and mechanical testing, a variety of morphological and densitometric measurements were made. Simple linear regression models revealed that trabecular density measurements acquired using pQCT showed a slightly stronger correlation with failure load than aBMD, but the inclusion of these density parameters in the multiple linear regression models made little, if any, improvement to the goodness of fit. The multiplication of the trabecular density by the cross-sectional area of the vertebral body significantly improved its correlation with failure load. Therefore, the prediction of failure load could be significantly improved by the measurement of these two simple parameters in clinic using a pQCT machine.

Additionally, a multiple linear regression model was created for the explanation of failure load using DXA aBMD and two geometric parameters (volume and cortical area). The fit of this model ($R^2 = 0.725$) was not significantly different from the trabecular density times area model previously described. The multiple linear regression model was improved by investigating the parameters that best explain stress at

failure. This model was very well fit ($R^2 = 0.871$) by the geometric variables selected and indicated that the height of the vertebral body as well as the cortex concavity are both significant factors in the explanation of stress at failure. Both of these parameters could be readily attained using existing DXA machines in clinic. As current clinical DXA examinations produce a projectional image of the vertebral area, measuring the cortex concavity and vertebral height would be a quick and easy way to significantly improve the prediction of bone strength. The parameters described in this study provide an insight into the factors besides bone density that contribute to bone strength. While this study involved a small number of samples, a foundation has been provided to support future work which could corroborate these findings and lead to the development of improved techniques for the diagnosis of osteoporosis.

## 5.2   Future Work

The objectives of this thesis work included clarification of the relationship between bone mineral density and strength, as well as the examination of geometrical factors that may be incorporated with density measurements in order to improve the explanation of bone strength. The correlations found between bone density and strength were consistent with those given in the literature, but the small number of samples available for this study limited the ability to draw conclusions about the validity of other studies based on the current one. While a significant improvement was made by the construction of multiple regression models, at least 28% of the variance

of failure load and 13% of the variance of stress at failure remain unexplained. These results indicate that further study of these relationships is warranted. The contribution of the cortical shell was a parameter of interest in the current study, particularly due to the wide variation of its contribution to compressive strength presented in the literature [43, 60]. Unfortunately, the presence of osteophytes on nearly half of the samples prevented accurate measurements of cortical area, thickness and density from being attained using available imaging techniques. Further dissection may allow manual geometric measurements of the cortical shell to be made such that they could be incorporated into the data set constructed in this study. The osteophytes were not assessed quantitatively in the current study but numerically characterizing them and relating these findings to vertebral strength may be an interesting area for further investigation.

Useful and well-fit multiple regression models were constructed for both failure load and stress at failure in this study. In order to simplify the analysis of the results, the models were restricted to a few key variables and linear data fitting techniques were used. It should also be noted that in multiple linear regression it is assumed that each of the X variables are independent of each other and have a normal distribution. The validity of this assumption cannot be verified with the small dataset available in this study. It is likely that expanding the number of coefficients in the model and applying other data fitting techniques would give better insight into the true nature of

bone strength. Step-wise regression or multivariate techniques may allow the missing data to be accommodated and finite element analysis may allow the significance of different parameters to be verified. Finite element techniques may allow the findings of this study to be further analyzed such that the reasons why certain parameters were found to be important in this study may be better understood. Finally, many other aspects of bone strength are being investigated in tandem to the structural property approach. Many researchers have chosen to investigate the microstructural properties of vertebrae, particularly the microarchitecture of the trabeculae. Still others explore the intrinsic material properties of bone by testing specimens of controlled dimensions rather than entire anatomic structures. The knowledge acquired in all of these methodologies is critical to attaining an accurate understanding of bone strength. Only when a way to integrate these different viewpoints is found will we truly be able to see the big picture.

# References

[1] P. Brinckmann, M. Biggemann, and D. Hilweg. Prediction of the compressive strength of human lumbar vertebrae. *Clinical Biomechanics*, 4:S1–S27, 1989.

[2] J.M. Buckley, K. Loo, and J. Motherway. Comparison of quantitative computed tomography-based measures in predicting vertebral compressive strength. *Bone*, 40(3):767–774, 2007.

[3] E.N. Ebbesen, J.S. Thomsen, H. Beck-Nielsen, H.J. Nepper-Rasmussen, and L. Mosekilde. Lumbar vertebral body compressive strength evaluated by dual-energy x-ray absorptiometry, quantitative computed tomography, and ashing. *Bone*, 25(6):713–724, 1999.

[4] S.J. Edmondston, K.P. Singer, R.E. Day, P.D. Breidahl, and R.I. Price. In-vitro relationships between vertebral body density, size, and compressive strength in the elderly thoracolumbar spine. *Clinical Biomechanics*, 9(3):180–186, 1994.

[5] S.J. Edmondston, K.P. Singer, R.E. Day, R.I. Price, and P.D. Breidahl. Ex vivo estimation of thoracolumbar vertebral body compressive strength: The relative contributions of bone densitometry and vertebral morphometry. *Osteoporosis International*, 7(2):142–148, 1997.

[6] T. Hansson, B. Roos, and A. Nachemson. The bone-mineral content and ultimate compressive strength of lumbar vertebrae. *Spine*, 5(1):46–55, 1980.

[7] M. Moro, A.T. Hecker, M.L. Bouxsein, and E.R. Myers. Failure load of thoracic vertebrae correlates with lumbar bone-mineral density measured by dxa. *Calcified tissue international*, 56(3):206–209, 1995.

[8] K. Singer, S. Edmondston, R. Day, P. Breidahl, and R. Price. Prediction of thoracic and lumbar vertebral body compressive strength - correlations with bone-mineral density and vertebral region. *Bone*, 17(2):167–174, 1995.

[9] D.D. Cody, S.A. Goldstein, M.J. Flynn, and E.B. Brown. Correlations between vertebral regional bone-mineral density (rbmd) and whole bone-fracture load. *Spine*, 16(2):146–154, 1991.

[10] X.G. Cheng, G. Lowet, S. Boonen, P.H.F. Nicholson, P. Brys, J. Nijs, and J. Dequeker. Assessment of the strength of proximal femur in vitro: Relationship to femoral bone mineral density and femoral geometry. *Bone*, 20(3):213–218, 1997.

[11] M.W. Devereaux. Anatomy and examination of the spine. *Neurologic Clinics*, 25(2):331–351, 2007.

[12] V.C. Mow and H.C. Wilson, editors. *Basic orthopaedic biomechanics*, volume 2nd. Lippincott Williams & Wilkins, New York, 1997.

[13] H. Gray. *Gray's Anatomy: Anatomy, descriptive and surgical.* Running Press Book Publishers, Philadelphia, 1974.

[14] C.M.(Christian M.) Langton and Christopher F. Njeh. *The physical measurement of bone.* Institute of Physics Pub., Philadelphia, 2004.

[15] Y.H. An and R.A. Draughn, editors. *Mechanical Testing of Bone and the Bone-Implant Interface.* CRC Press, New York, 1999.

[16] C.M. Bono and T.A. Einhorn. Overview of osteoporosis: pathophysiology and determinants of bone strength. *European Spine Journal*, 12:S90–S96, 2003.

[17] C.H. Turner and D.B. Burr. Basic biomechanical measurements of bone - a tutorial. *Bone*, 14(4):595–608, 1993.

[18] T. Beck. Measuring the structural strength of bones with dual-energy x-ray absorptiometry: principles, technical limitations, and future possibilities. *Osteoporosis International*, 14:S81–S88, 2003.

[19] NIH Consensus Development Panel on Osteoporosis Prevention Diagnosis and Therapy. Osteoporosis prevention, diagnosis and therapy, 2001.

[20] D.A. Hanley. Prevention and management of osteoporosis: Consensus statements from the scientific advisory board of the osteoporosis society of canada. *Canadian Medical Association Journal*, 156(1):23–23, 1997.

[21] R. Goeree, D. Pettitt, B. O'Brien, and et al. An assessment of the burden of illness due to osteoporosis in canada. *J.Soc.Obstet.Gynaecol.*, 18(Supplement):15–24, 1996.

[22] L.R. Hedlund, J.C. Gallagher, C. Meeger, and S. Stoner. Change in vertebral shape in spinal osteoporosis. *Calcified tissue international*, 44(3):168–172, 1989.

[23] European Vertebroplasty Research Team. Vertebral fractures, http://www.everest-group.eu, 2006.

[24] S.L. Silverman. The clinical consequences of vertebral compression fracture. *Bone*, 13:S27–S31, 1992.

[25] D.P. Lindsey, M.J. Kim, M. Hannibal, and T.F. Alamin. The monotonic and fatigue properties of osteoporotic thoracic vertebral bodies. *Spine*, 30(6):645–649, 2005.

[26] C. Cooper, E.J. Atkinson, W.M. Ofallon, and L.J. Melton. Incidence of clinically diagnosed vertebral fractures - a population-based study in rochester, minnesota, 1985-1989. *Journal of Bone and Mineral Research*, 7(2):221–227, 1992.

[27] A.W. Friedman. Important determinants of bone strength - beyond bone mineral density. *Jcr-Journal of Clinical Rheumatology*, 12(2):70–77, 2006.

[28] K.W. Lyles et al. Zoledronic acid and clincial fractures and mortality after hip fracture. *New England Journal of Medicine*, Epub ahead of print, 2007.

[29] P. McDonnell, P.E. McHugh, and D. O'Mahoney. Vertebral osteoporosis and trabecular bone quality. *Annals of Biomedical Engineering*, 35(2):170–189, 2007.

[30] M. Delaney. Understanding bone strength - determinants and treatment effects. *Endocrinologist*, 16(2):79–85, 2006.

[31] National Osteoporosis Foundation. *Physician's guide to prevention and treatment of osteoporosis*. National Osteoporosis Foundation, Washington, D.C., 2003.

[32] E.S. Siris, Y.T. Chen, T.A. Abbott, E. Barrett-Connor, P.D. Miller, L.E. Wehren, and M.L. Berger. Bone mineral density thresholds for pharmacological intervention to prevent fractures. *Archives of Internal Medicine*, 164(10):1108–1112, 2004.

[33] K.L. Stone, D.G. Seeley, L.Y. Lui, J.A. Cauley, K. Ensrud, W. Browner, M.C. Nevitt, and S.R. Cummings. Bmd at multiple sites and risk of fracture of multiple types: Long-term results from the study of osteoporotic fractures. *Journal of Bone and Mineral Research*, 18(11):1947–1954, 2003.

[34] P. Augat, T. Fuerst, and H.K. Genant. Quantitative bone mineral assessment at the forearm: A review. *Osteoporosis International*, 8(4):299–310, 1998.

[35] H.K. Genant, K. Engelke, T. Fuerst, C.C. Gluer, S. Grampp, S.T. Harris, M. Jergas, T. Lang, Y. Lu, S. Majumdar, A. Mathur, and M. Takada. Noninvasive assessment of bone mineral and structure: State of the art. *Journal of Bone and Mineral Research*, 11(6):707–730, June 1996.

[36] H. Granhed, R. Jonson, and T. Hansson. Mineral-content and strength of lumbar vertebrae - a cadaver study. *Acta Orthopaedica Scandinavica*, 60(1):105–109, 1989.

[37] N.B. Watts. Fundamentals and pitfalls of bone densitometry using dual-energy x-ray absorptiometry (dxa). *Osteoporosis International*, 15(11):847–854, 2004.

[38] R. Mazess, C.H. Chesnut, M. McClung, and H. Genant. Enhanced precision with dual-energy x-ray absorptiometry. *Calcified tissue international*, 51(1):14–17, 1992.

[39] S. Butz, C. Wuster, C. Scheidtnave, M. Gotz, and R. Ziegler. Forearm bmd as measured by peripheral quantitative computed-tomography in a german reference population. *Osteoporosis International*, 4(4):179–184, 1994.

[40] W.A. Kalender. Principles and applications of spiral ct. *Nuclear Medicine and Biology*, 21(5):693–699, 1994.

[41] L. Mosekilde, S.M. Bentzen, G. Ortoft, and J. Jorgensen. The predictive value

of quantitative computed-tomography for vertebral body compressive strength and ash density. *Bone*, 10(6):465–470, 1989.

[42] S.A.V. Eriksson, B.O. Isberg, and J.U. Lindgren. Prediction of vertebral strength by dual photon-absorptiometry and quantitative computed-tomography. *Calcified tissue international*, 44(4):243–250, 1989.

[43] R.J. Mcbroom, W.C. Hayes, W.T. Edwards, R.P. Goldberg, and A.A. White. Prediction of vertebral body compressive fracture using quantitative computed-tomography. *Journal of Bone and Joint Surgery-American Volume*, 67A(8):1206–1214, 1985.

[44] A. Nachemson and G. Elfstrm. Intravital dynamic pressure measurements in lumbar discs. a study of common movements, maneuvers and exercises. *Scand J Rehabil Med Suppl*, 1:1–40, 1970.

[45] T.P.J. Leskinen, H.R. Stalhammar, I.A.A. Kuorinka, and J.D.G. Troup. A dynamic analysis of spinal-compression with different lifting techniques. *Ergonomics*, 26(6):595–604, 1983.

[46] L. Kazarian and G.A. Graves. Compressive strength characteristics of the human vertebral centrum. *Spine*, 2:1–14, 1977.

[47] J.K. Weaver and J. Chalmers. Cancellous bone: Its strength and changes with

aging and an evaluation of some methods for measuring its bone mineral content. *J Bone Miner Res*, 48A:289–298, 1966.

[48] O. Beck J.S. Bell, G.H. Dunbar and A. Gibb. Variations in strength of vertebrae with age and their relation to osteoporosis. *Calcif Tissue Res*, 1(75):86–, 1967.

[49] S.J. Edmondston, K.P. Singer, R.E. Day, P.D. Breidahl, and R.I. Price. Formalin fixation effects on vertebral bone-density and failure mechanics - an in-vitro study of human and sheep vertebrae. *Clinical Biomechanics*, 9(3):175–179, 1994.

[50] S.K. Eswaran, A. Gupta, M.F. Adams, and T.M. Keaveny. Cortical and trabecular load sharing in the human vertebral body. *Journal of Bone and Mineral Research*, 21(2):307–314, 2006.

[51] N. Yoganandan, F.A. Pintar, B.D. Stemper, J.L. Baisden, R. Aktay, B.S. Shender, and G. Paskoff. Bone mineral density of human female cervical and lumbar spines from quantitative computed tomography. *Spine*, 31(1):73–76, 2006.

[52] M.J. Fagan, S. Julian, and A.M. Mohsen. Finite element analysis in spine research. *Proceedings of the Institution of Mechanical Engineers Part H-Journal of Engineering in Medicine*, 216(H5):281–298, 2002.

[53] K. Imai, I. Ohnishi, M. Bessho, and K. Nakamura. Nonlinear finite element

model predicts vertebral bone strength and fracture site. *Spine*, 31(16):1789–1794, 2006.

[54] V. Gilsanz, M.L. Loro, T.F. Roe, J. Sayre, R. Gilsanz, and E.E. Schulz. Vertebral size in elderly women with osteoporosis - mechanical implications and relationship to fractures. *Journal of Clinical Investigation*, 95(5):2332–2337, 1995.

[55] M. Krismer, C. Haid, H. Behensky, P. Kapfinger, F. Landauer, and F. Rachbauer. Motion in lumbar functional spine units during side bending and axial rotation moments depending on the degree of degeneration. *Spine*, 25(16):2020–2027, 2000.

[56] F. Linde and H.C.F. Sorensen. The effect of different storage methods on the mechanical-properties of trabecular bone. *Journal of Biomechanics*, 26(10):1249–1252, 1993.

[57] Y.B. Duan, C.H. Turner, B.T. Kim, and E. Seeman. Sexual dimorphism in vertebral fragility is more the result of gender differences in age-related bone gain than bone loss. *Journal of Bone and Mineral Research*, 16(12):2267–2275, 2001.

[58] M.J. Silva and L.J. Gibson. Modeling the mechanical behavior of vertebral trabecular bone: Effects of age-related changes in microstructure. *Bone*, 21:191–199, 1997.

[59] L. Eriksson, E. Johansson, N. Kettaneh-Wold, and S. Wold. *Multi- and Megavariable Data Analysis - Principles and Applications.* Umetrics, Umea, Sweden, 2001.

[60] Edward Rockoff, S.D. Sweet and Jeffery Bleustein. The relative contribution of trabecular and cortical bone ot the strength of human lumbar vertebrae. *Calcif Tissue Res*, 3:163–175, 1969.

# Appendix I: DXA algorithm descriptions

**Contour Mode 2**

This contour mode defines the outer edge of the bone by an iterative technique. First, all of the voxels with a value below Threshold 1 (169 mg/cm3) are removed from the image in order to eliminate the soft tissue. Using the threshold defined for cortical bone (711 mg/cm3), the first voxel of the bone edge is located. The algorithm compares the neighbouring voxels to the first voxel, selecting the voxels that fall above the cortical threshold. This process continues until the algorithm has returned to the first voxel of the bone edge and the entire cortical shell has been defined.

**Peel Mode 2**

This algorithm separates the voxels into trabecular bone and subcortical bone. Threshold 2 is utilized in this algorithm as the transition point from trabecular to subcortical bone. All voxels falling above Threshold 2 (400 mg/cm3) are defined as subcortical. This is the recommended peel mode for specimens with irregular cortical thickness.

For more details on the algorithms used in pQCT analysis, the reader is referred to the Stratec XCT Research Manual.
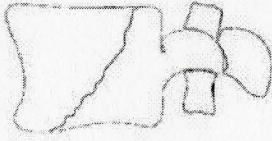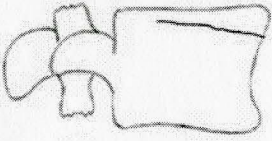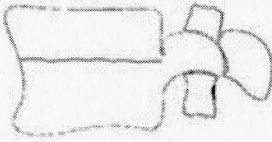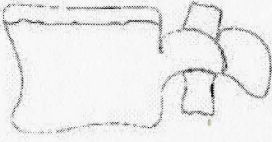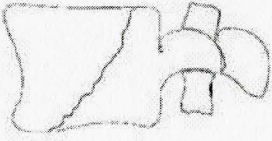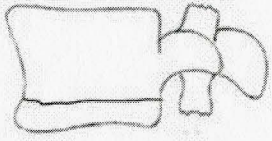
# Appendix II: Load cell calibration plot
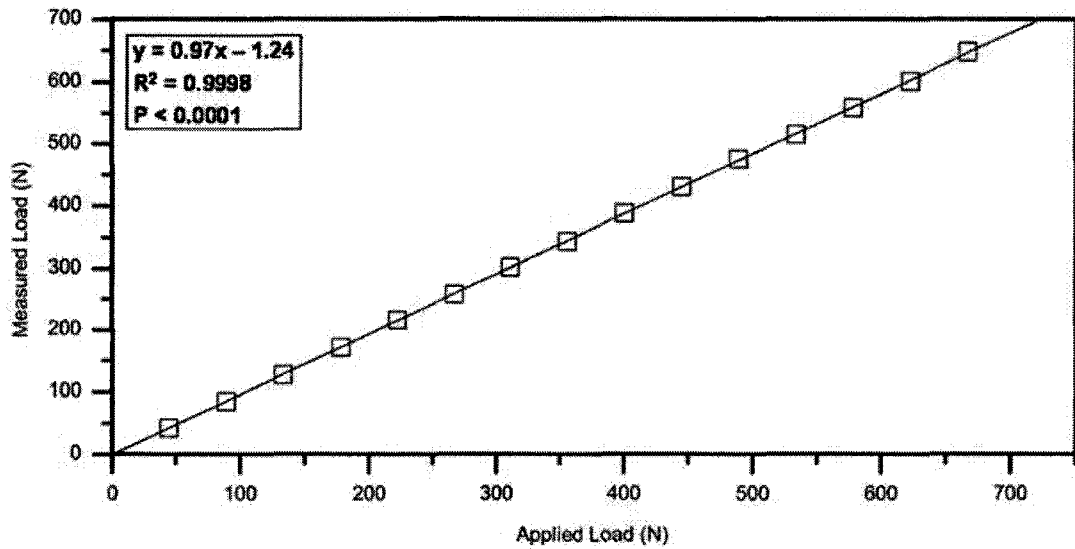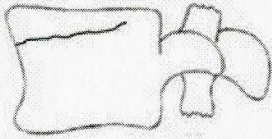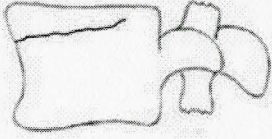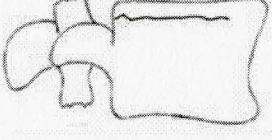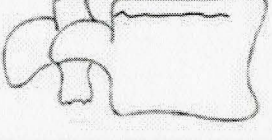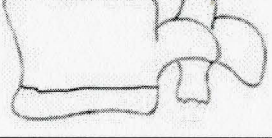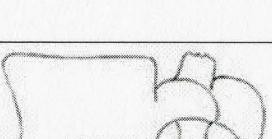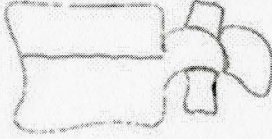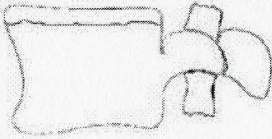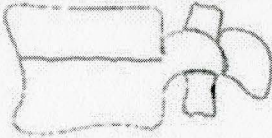
# Appendix III: Condition of intervertebral discs

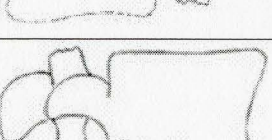| Specimen | | Disc Condition | | | |
|---|---|---|---|---|---|
| | | Proximal | | Distal | |
| Spine | Vertebra | Grade | Notes | Grade | Notes |
| 1 | T10 | 2 | | 2/3 | |
| 2 | T2 | 2/3 | | 2/3 | |
| | T4 | 4 | | 3 | |
| | T6 | 3 | | 2/3 | |
| | T8 | 2 | | 3 | |
| | T10 | 2/3 | | 3 | |
| 3 | T2 | 2 | | 2 | |
| | T4 | 2/3 | | 2/3 | |
| | T6 | 2 | Minor osteophyte on anterior, left lateral region of disc | 2 | Osteophyte on anterior, target region of disc |
| | T8 | 1/2 | | 1/2 | |
| | T10 | 1/2 | | 2 | |
| 4 | T6 | 2/3 | | 3 | |
| | T8 | 4 | Osteophyte on anterior, right lateral region of disc | 4 | Osteophyte on anterior, right lateral region of disc |
| | T10 | 3/4 | | 4 | |
| | T12 | 3 | Osteophyte on anterior, right lateral region of disc | 3 | Osteophyte on anterior, right lateral region of disc |
| | L2 | 2/3 | Osteophyte on anterior, right lateral region of disc | 2 | |
| 5 | T3 | 3 | Minor osteophyte on target anterior region of disc | 3 | |
| | T5 | 2/3 | | 3 | |
| | T7 | 2 | | 2/3 | Osteophyte on anterior, right lateral region of disc |
| | T9 | 4 | Significant osteophytes completely covering anterior region of disc | 1/2 | Osteophyte on anterior, right lateral region of disc |
| | T11 | 2 | Minor osteophyte on anterior, lateral region of disc | Fused | Bony growth bridging T11 to T12 |

# Appendix IV: Characteristics of target vertebra failure

| Specimen | | Failure Load (N) | Schematic | Description |
|---|---|---|---|---|
| Spine | Vertebra | | | |
| 1 | T10 | 2491 | | Wedge type fracture with crack visible from left view |
| 2 | T2 | 1411 | | Wedge type fracture with crack visible from right view, initiating at anterior distal endplate and extending towards the rear |
| | T4 | 1539 | | Wedge type fracture with crack near mid-body, visible from left view |
| | T6 | 1170 | | Wedge type fracture with crack near proximal endplate, visible from left view |
| | T8 | 1160 | | Wedge type fracture with crack visible from left side, extending from superior, posterior region to inferior, anterior region |
| | T10 | 1199 | | Wedge type fracture with crack near distal endplate, visible from left view |
| 3 | T2 | 1083 | | Wedge type fracture with crack near mid-body, visible from left view |
| | T4 | 1211 | | Crush type fracture with crack near mid-body, visible from left view |

| Specimen | | Failure Load (N) | Schematic | Description |
| Spine | Vertebra | | | |
| --- | --- | --- | --- | --- |
| 3 | T6 | 1338 |  | Wedge type fracture with crack visible from left view, initiating at anterior, proximal endplate, extending slightly upwards |
| | T8 | 1178 |  | Wedge type fracture with crack visible from left view, initiating at anterior, proximal endplate, extending slightly upwards |
| | T10 | 1795 |  | Wedge type fracture with crack near mid-body, visible from left view |
| 4 | T6 | 3511 |  | Wedge type fracture with crack visible from right view initiating near anterior, proximal endplate |
| | T8 | 4436 |  | Crush type fracture with crack near proximal endplate, visible from right view |
| | T10 | 3631 |  | Wedge type fracture with crack near distal endplate, visible from left view |
| | T12 | 5221 | | Crush type fracture with no crack visible on HCT image |
| | L2 | 3924 |  | Wedge type fracture with crack near distal endplate, visible from left view |
| 5 | T3 | 2647 |  | Wedge type fracture with crack near proximal endplate, visible from view |
| | T5 | 3608 |  | Wedge type fracture with crack visible from right view initiating at posterior distal endplate and extending forward |

| Specimen | | Failure Load (N) | Schematic | Description |
| --- | --- | --- | --- | --- |
| Spine | Vertebra | | | |
| 5 | T7 | 5592 | | Wedge type fracture with crack near mid-body, visible from left view |
| | T9 | 4289 | | Wedge type fracture with crack near proximal endplate, visible from left view |
| | T11 | 8280 | | Wedge type fracture with crack near mid-body, visible from left view |